Genetically diverse mouse models of SARS-CoV-2 infection reproduce clinical variation in type I interferon and cytokine responses in COVID-19.

Shelly J. Robertson[1], Olivia Bedard[2], Kristin L. McNally[1], Carl Shaia[3], Chad Clancy[3], Matthew Lewis[1], Rebecca M. Broeckel[1], Abhilash I. Chiramel[4], Jeffrey G. Shannon[1], Gail L. Sturdevant[1], Rebecca Rosenke[3], Sarah L. Anzick[5], Elvira Forte[2,†], Christoph Preuss[2], Candice N. Baker[2], Jeffrey Harder[2], Catherine Brunton[2], Steven Munger[2], Daniel P. Bruno[5], Justin B. Lack[5], Jacqueline M. Leung[5], Amirhossein Shamsaddini[5], Paul Gardina[5], Daniel E. Sturdevant[5], Jian Sun[5], Craig Martens[5], Steven M. Holland[6], Nadia A. Rosenthal[2,7]* and Sonja M. Best[1]*

[1]Laboratory of Persistent Viral Diseases, Rocky Mountain Laboratories, National Institute of Allergy and Infectious Diseases, NIH; Hamilton MT USA

[2]The Jackson Laboratory; Bar Harbor Maine USA

[3]Rocky Mountain Veterinary Branch, Rocky Mountain Laboratories, National Institute of Allergy and Infectious Diseases, NIH; Hamilton MT USA

[4]Boehringer Ingelheim, Ingelheim, Germany

[5]Research Technologies Branch, National Institute of Allergy and Infectious Diseases, NIH; USA

[6]Division of Intramural Research, National Institute of Allergy and Infectious Diseases, NIH; Bethesda MD USA

[7]National Heart and Lung Institute; Imperial College London

[†]Springer Nature, New York USA

*co-corresponding authors

One Sentence Summary

Genetically diverse mice model a spectrum of clinically relevant innate immune responses to SARS-CoV-2 infection.

ABSTRACT

Inflammation in response to severe acute respiratory syndrome coronavirus-2 (SARS-CoV-2) infection drives severity of coronavirus disease 2019 (COVID-19) and is influenced by host genetics. To understand mechanisms of inflammation, animal models that reflect genetic diversity and clinical outcomes observed in humans are needed. We report a mouse panel comprising the genetically diverse Collaborative Cross (CC) founder strains crossed to human ACE2 transgenic mice (K18-hACE2) that confers susceptibility to SARS-CoV-2. Infection of CC x K18-hACE2 resulted in a spectrum of survival, viral replication kinetics, and immune profiles. Importantly, in contrast to the K18-hACE2 model, early type I interferon (IFN-I) and regulated proinflammatory responses were required for control of SARS-CoV-2 replication in PWK x K18-hACE2 mice that were highly resistant to disease. Thus, virus dynamics and inflammation observed in COVID-19 can be modeled in diverse mouse strains that provide a genetically tractable platform for understanding anti-coronavirus immunity.

INTRODUCTION

The COVID-19 pandemic continues to pose a global threat to public health, due in part to sequential evolution of new variants of concern (VOC) selected to evade immunity generated from previous infection or vaccination. The extreme variability in patient responses to infection, ranging from asymptomatic to life-threatening illness[1-3], remains only partially understood. In addition, persistent post-COVID health problems can be severe and include a significant risk for future morbidity and mortality[4]. The variability in disease presentation is dependent on genetic polymorphisms, age, sex and the presence of underlying conditions[1,5,6], underscoring the need for research models that reflect the diverse biology and pathology of SARS-CoV-2 infection in order to provide optimal platforms for preclinical development of novel therapeutic strategies.

Type I interferon (IFN-I) is essential for control of virus replication, but its functions in COVID-19 are complex and poorly understood, with evidence for roles in both protective and pathogenic host response[7]. Success of IFN-I in controlling virus replication and orchestrating an effective inflammatory response may relate to the timing of IFN-I induction relative to peak SARS-CoV-2 replication, the intensity of IFN-I expression and the kinetics of response resolution[8]. In humans, favorable outcomes of COVID-19 have been associated with robust early IFN-I responses

57 that are subsequently resolved along with other disease signs[9]. However, the more severe manifestations of COVID-
58 19, including reduced oxygen saturation, higher inflammatory responses and lower anti-viral antibody responses,
59 have been observed in patients with either an early IFN-I response that fails to resolve[10], or an IFN-I response that is
60 substantially delayed relative to peak virus replication[11-14]. The roles of IFN-I in a pathogenic response may be
61 linked to failure of control of virus replication. However, late, or sustained IFN-I responses may drive pathogenesis
62 through failure to orchestrate an effective adaptive response, exacerbation of inflammatory monocyte responses and
63 inhibition of tissue repair[7,10]. In mice, loss of IFN-I signaling reduces inflammatory cell recruitment in the lung, but
64 a direct antiviral role of IFN-I is less clear[15,16]. Thus, additional experimental models are needed that inform how
65 timing, magnitude, and duration of innate immunity relative to virus replication dynamics determines virus
66 dissemination and whether inflammatory responses are protective or pathogenic.

67 Current mouse models of COVID-19 are important tools in understanding drivers of inflammatory responses and
68 pathology following infection with SARS-CoV-2, but are typically generated on invariant inbred backgrounds,
69 poorly reflecting the diversity of patient outcomes and the impact of host genetics on SARS-CoV-2 infection and
70 response to treatment. Mice humanized for the main cellular receptor for SARS-CoV-2 entry, angiotensin
71 converting enzyme 2 (ACE2)[17], have been essential pre-clinical infection models[18]. The most widely used model
72 carrying a human ACE2 gene (K18-hACE2) supports high early virus replication in lung epithelial cells, resulting in
73 inflammatory cell infiltration, interstitial edema and focal consolidation of the lung with rapid lethality following
74 virus dissemination to the central nervous system (CNS)[19-24]. However, this model on a standard C57BL/6J genetic
75 background does not reflect the wide variety of COVID-19 outcomes in humans[1,5,6]. Indeed, in the absence of
76 comparative models with different outcomes, it is not known what human response is being modeled by SARS-
77 CoV-2 infection of K18-hACE2 mice specifically regarding how IFN-I response dynamics relates to control of virus
78 replication and pathology.
79
80 To determine if incorporating genetic diversity could recapitulate the broad phenotypic variation observed in human
81 COVID-19, we crossed the K18-hACE2 strain to the genetically distinct inbred strains A/J, 129S1/SvImJ,
82 NOD/ShiLtJ, NZO/HILtJ, PWK/PhJ, CAST/EiJ, and WSB/EiJ that along with C57BL/6J comprise the CC founders.
83 Together, these strains represent 90% of the genetic diversity in *M. musculus* populations[25,26], and therefore can be
84 used to understand genetic regulation of complex immune responses. Notably, NOD/ShiLtJ and NZO/HILtJ mice

are commonly used in studies of diabetes and metabolic dysfunction, both factors contributing to COVID-19 severity[27]. In addition to the 8 CC founder strains, BALB/cJ and DBA/2J strains were included because BALB/cJ is widely used in infectious disease modelling, and DBA/2J is a founder strain for BXD strains also used in genetic mapping[28]. Here, we show that by using these genetically diverse mice we can model both early and delayed innate immune responses associated with differing control of virus replication kinetics and pathology in the lung, and formally demonstrate an effective antiviral role for IFN-I if produced early. These mice, therefore, represent invaluable tools to understand how IFN-I and proinflammatory responses are orchestrated to control SARS-CoV-2 replication and pathology.

RESULTS

Diverse outcomes of SARS-CoV-2 infection in CC x K18-hACE2 F1 mice

F1 progeny of CC founder x K18-hACE2 mice (hereafter abbreviated CC x K18-hACE2) were infected via intranasal inoculation with 10^3 plaque forming units (pfu) SARS-CoV-2 strain nCoV-WA1-2020, MN985325.1 and mice were monitored for 21 days. This virus dose is sub-uniformly lethal in the prototype K18-hACE2 strain (C57BL/6J background), resulting in 80-90% of mice reaching end-point criteria by 7 days post infection (dpi) (Fig. 1a). Infection was confirmed in all survivors by seroconversion to SARS-CoV-2 nucleoprotein. Comparative analysis of the eight CC x K18-hACE2 F1 cohorts documented a broad spectrum of weight loss and survival curves characteristic to each CC founder genotype, some of which were sex-specific. Highly sensitive strains included C57BL/6J and A/J x K18-hACE2 that lost approximately 20% of their starting weight between 4 and 7 dpi with no clear sex bias (Fig. 1a). In contrast, CC x K18-hACE2 from PWK, NZO, 129S1/J (Fig. 1b), BALB/cJ and DBA/2J (Fig. S1a, b) were comparatively resistant to clinical disease, generally losing 5-10% starting weight with ~80% of mice surviving infection. Finally, CC x K18-hACE2 of three strains (CAST, NOD, WSB) had marked sexual dimorphism, with CAST and NOD males susceptible to lethal disease, although differences in weight loss between sexes were not apparent (Fig. 1c). Yet another phenotype was observed in WSB x K18-hACE2, where infection was uniformly lethal in females. Weight loss in males began at 6 dpi, later than other groups, and surviving males exhibited sustained weight loss in contrast to the rapid weight gain associated with recovery of other CC x K18-hACE2 cohorts (Fig. 1c).

114 **Virus replication and dissemination in CCxK18-hACE2 F1 mice**

115 In K18-hACE2 mice, SARS-CoV-2 titers peak in the lung at 2-3 dpi and high titers of virus can be isolated from the
116 CNS which may contribute to lethality in this model[17,29]. Thus, virus replication kinetics were determined at 3 and 6
117 dpi in lung and brain of CC x K18-hACE2 cohorts (Fig. 2a, Fig. S1c). Sensitive founder strains C57BL/6J and A/J
118 F1 progeny showed high levels of infectious SARS-CoV-2 at 3 dpi in lung homogenates that was reduced by 1-2
119 $\log_{10}$ by 6 dpi with no differences between sexes. At 3 dpi, infectious virus was generally not recovered from the
120 CNS, but ~50% of K18-hACE2 and A/J x K18-hACE2 had high virus burden in the CNS by 6 dpi (10^6-10^8 pfu/g
121 tissue) suggesting significant virus dissemination outside of the lung. In contrast, peak lung virus titer in the most
122 resistant PWK x K18-hACE2 was 150-fold lower than the sensitive strains at 3 dpi and was below the limit of
123 detection at 6 dpi. Control of virus replication in PWK x K18-hACE2 was also evident in the CNS where detection
124 of infectious virus was sporadic. Interestingly, additional CC x K18-hACE2 classed as resistant had equivalent peak
125 viral titers in the lung to the sensitive K18-hACE2 and A/J F1 progeny, but they tended to control replication by 6
126 dpi to levels 1 $\log_{10}$ lower than sensitive mice and had less virus burden in the CNS. Finally, lung titers in (CAST,
127 NOD and WSB) x K18-hACE2 were not different between males and females despite differences in clinical severity
128 associated with sex. Relative expression of the K18-hACE2 transgene in lung was not different between genetic
129 backgrounds (Fig. S2b) and ACE2 distribution was not distinguishable between sensitive (K18-hACE2) and
130 resistant (PWK x K18-hACE2) mice by immunohistochemistry (Fig. S2c). Thus, CC x K18-hACE2 can be further
131 stratified into a) sensitive with high sustained virus replication in lung and CNS (C57BL/6J, A/J), b) resistant with
132 lower peak virus titer or earlier control of replication in the lung and no or low dissemination to other organs (PWK,
133 NZO, 129S1/J), and c) sex-biased outcomes in survival independent of virus titer in the lung suggesting a sex-based
134 difference in host response (CAST, NOD, WSB). Together, these data demonstrate that major differences in the
135 dynamics of SARS-CoV-2 replication and host sensitivity to disease observed in humans can be modeled through
136 use of genetically diverse mouse strains (Summarized in Table S1).

137

138 **Histopathology in lung and brain from SARS-CoV-2 -infected CC x K18-hACE2 F1 progeny**

139 The general pathological changes in SARS-CoV-2-infected K18-hACE2 mice were similar to those previously
140 described [19,23,24,30] although varied in severity (Fig. 2b-d). Inflammatory infiltrates evident by 3 dpi included
141 perivascular lymphocytes with alveolar septa thickened by neutrophils, macrophages, and edema. At 6 dpi,

142 pulmonary pathology was multifocal, and consistent with interstitial pneumonia including type II pneumocyte
143 hyperplasia, septal, alveolar and perivascular inflammation comprised of lymphocytes, macrophages and
144 neutrophils, with alveolar fibrin and edema evident. Bronchiolar pathology was not observed in these mice. Lung
145 pathology was classified as none, mild (rare scattered inflammatory foci), moderate (coalescing inflammatory foci)
146 or severe (widespread, large inflammatory foci) as exemplified in Fig. 2c. Surprisingly, most resistant strains and
147 those with sex bias tended to have higher pneumonia scores in lungs compared to the sensitive K18-hACE2 and A/J
148 x K18-hACE2 (Fig. 2d). Lung distribution of viral RNA was limited to type I and II pneumocytes in all strains (Fig.
149 2b, Fig. 5b). Importantly, these data suggest that lung pathology can be exacerbated in the context of effective
150 control of SARS-CoV-2 replication but still be associated with rapid recovery, as modeled in PWK x K18-hACE2
151 and NZO x K18-hACE2. In contrast, higher pathology scores associated with uncontrolled virus replication in the
152 lung and higher sensitivity to severe disease can be modeled by in WSB x K18-hACE2.
153
154 CNS pathology was scored as present or absent, as it generally consisted of subtle inflammatory foci, including
155 perivascular cuffing and gliosis associated with necrotic cells observed in K18-hACE2 and DBA x K18-hACE2
156 males (Fig. S3a-c, g). However, pathology in the CNS of CAST x K18-hACE2 was striking in that microthrombi
157 were evident in capillaries with extensive hemorrhage in the absence of encephalitis. Although microthrombi were
158 associated with viral RNA distribution in the same area (Fig. S3d-f), microhemorrhage was not observed as
159 extensively in infected K18-hACE2 mice. In addition, infection with 10^3 pfu SARS-CoV-2 was uniformly lethal in
160 male CAST x K18-hACE2, despite these mice having some of the lowest levels of pathology in the lung at 6 dpi of
161 all mice examined. Thus, CAST x K18-hACE2 mice may be a suitable model for examination of microthrombus
162 formation sometimes observed in severe human COVID-19[31-33].
163
164 **Distinct timing and amplitude of cytokine and chemokine induction in CC x K18-hACE2 F1 mice**
165 In-depth longitudinal analyses of immune responses in patients with COVID-19 have defined immunological
166 correlates of disease outcome[8,10,12,34-44]. In addition to high early IFN responses, moderate COVID-19 is associated
167 with increased plasma levels of a core of pro-inflammatory cytokines, chemokines and growth factors (e.g., IL-1a,
168 IL-1β, IFNα, IL-12p70, and IL-17A) that are effectively resolved during infection[10]. In contrast, severe COVID-19
169 includes sustained expression of these markers with additional signatures including IL-6, IL-10, IL-18, IL-23, TNF,

170 and eotaxin among others suggesting that specific timing and failure to resolve inflammatory responses are
171 important factors in disease progression[10].
172
173 In SARS-CoV-2-infected CC x K18-hACE2, cytokines and chemokines were quantified in the serum and
174 bronchoalveolar lavage fluid (BAL) at 3 and 6 dpi. Cytokine levels were much higher in BAL than in serum (Fig.
175 S4a-c; individual data points are provided in Figs. S5-S7). IFNα was variably induced at 3 dpi in all crosses with
176 K18-hACE2 (Fig. 3a and Fig. S1e). Strikingly, K18-hACE2 and CC x K18-hACE2 of A/J, CAST and NOD
177 produced relatively low IFNα compared to PWK, NZO, 129S1/J and WSB that produced 2- to 10-fold higher levels.
178 At 3 dpi, IFNα production was similar in males and females within each strain except for PWK x K18-hACE2
179 males produced significantly higher levels than females, and in DBA x K18-hACE2 where females were higher
180 (Fig. S1d). Importantly, high early IFNα expression at 3 dpi was resolving by 6dpi in resistant ((PWK, NZO and
181 129S1/J) x K18-hACE2) that most effectively controlled virus replication in the lung and CNS. In comparison, low
182 levels of IFNα were observed in K18-hACE2 mice at 3 and 6 dpi despite high early virus burden in the lung and
183 failure to control disseminating infection by 6 dpi (Fig. 3b, c; Fig. S5). Thus, PWK x K18-hACE2 may represent a
184 model of effective induction and resolution of IFN responses associated with viral control. A third distinct
185 phenotype was observed in WSB x K18-hACE2 that had high IFNα expression in BAL at 3 dpi equivalent to PWK
186 x K18-hACE2, but these mice did not control virus replication in the lung as effectively as PWK F1 mice and had
187 sustained weight loss in surviving individuals. Indeed, WSB x K18-hACE2 produced some of the highest IFNα
188 among all genetic backgrounds at 3 dpi (Fig. 3a) along with high levels of cytokines and chemokines (Fig. S4a-c),
189 which may be consistent with significant weight loss observed in both sexes (Fig. 1c). In addition, WSB x K18-
190 hACE2 had equivalent lung virus titers to K18-hACE2 mice at 3 and 6 dpi, but virus was only sporadically
191 recovered from brain (Fig. 2a). Despite similarities in virus burden between sexes, female WSB x K18-hACE2 mice
192 were significantly more sensitive to severe clinical disease (Fig. 1c) and lung pathology (Fig. 2d). Thus, the WSB
193 strain background may model the situation where high IFN responses are not associated with viral control and
194 contribute to pathogenesis.
195
196 To further compare the relative expression of immune effectors in BAL, unsupervised hierarchical cluster analysis
197 was performed on data from sensitive (K18-hACE2 and A/J x K18-hACE2) and three resistant strains that did not

198 show a sex bias ((PWK, NZO, 129S1/J) x K18-hACE2). SARS-CoV-2-infected mice grouped into four general
199 clusters each with distinct profiles of cytokine and chemokine expression. As shown in Fig. 3d, Cluster 1 was
200 comprised of resistant mice at 3 dpi that expressed proinflammatory cytokine IL-6, TH1 cytokines (IL-12p70, IFNγ,
201 IL-27), inflammasome associated cytokine (IL-1beta and IL-18) and chemokines (CXCL10, Gro-α/KC, CCL2,
202 CCL3, CCL4, CCL5, CCL7 and CXCL2) (designated as Group A). At 6 dpi, some Group A cytokines were
203 resolving (IL-6, IL-27, CCL2 and CXCL10) (Fig. 3e; Table S2; Table S3) while IL-2, IL-4, IL-5, IL-13, IL-18, IL-
204 1b, GM-CSF, eotaxin, TNF-α, IFN-γ, and IL10 (designated as Group B) were added to the cytokine signature in
205 resistant mice (Fig. 3d, Cluster 2). Interestingly, resistant PWK and NZO x K18-hACE2 mice generally exhibited a
206 unique profile characterized by tempered levels of Group A and Group B along with high production of Gro-α/KC,
207 CCL7, CXCL10, CCL2, eotaxin, and IFNγ, at 6 dpi, a timepoint coincident with the most efficient clearance of virus
208 from the lung (Cluster 4). In contrast, sensitive strains generally failed to produce Group A cytokines at 3 dpi
209 (Cluster 3) and if induced, production of both Group A and Group B mediators occurred at the later timepoint (Fig.
210 3d, Cluster 2). In contrast, sensitive F1 progeny produced significantly higher levels of IL-10 (immune suppressive
211 cytokine) and CCL4 (monocyte and neutrophil recruiting chemokine) at 6 dpi compared to resistant F1(Fig. 3e;
212 Table S2).
213
214 **Type I IFN signaling controls early SARS-CoV-2 replication and coordinates inflammatory responses in**
215 **PWK x K18-hACE2.**
216 A correlation coefficient analysis was performed to determine the relationship between IFNα and other immune
217 mediators, focusing on sensitive (K18-hACE2) and resistant (PWK x K18-hACE2) mice. In PWK x K18-hACE2,
218 high levels of IFNα at 3 dpi positively correlated with a small subset of cytokines (IFNγ, IL-12p70, IL-6, IL-27 and
219 CCL5) and negatively correlated with IL-10, CXCL10 and CXCL2 (Fig. 3f). In K18-hACE2 mice, low IFNα
220 production correlated with low expression of these same immune mediators along with pro-inflammatory TNFα and
221 IL-18, and immune cell recruiting chemokines (eotaxin, CCL3 and CCL4). Although IFNα expression was resolved
222 to near basal levels in both sensitive and resistant F1 mice at 6 dpi (Fig. 3b, c) expression correlations between
223 immune mediators increased in sensitive K18-hACE2, but generally decreased in resistant PWK x K18-hACE2
224 (Fig. 3g), consistent with high dysregulation in K18-hACE2.
225

226 To obtain an unbiased, global assessment of host responses in a direct comparison between resistant and sensitive
227 mouse models, we performed Visium spatial transcriptomics on lungs from male K18-hACE2 and PWK x K18-
228 hACE2 at 0 (naïve), 3 and 6 dpi. Confidence calling of cell types suggested that a significant proportion of Visium
229 spots captured transcriptional signatures representing more than one cell type, predominantly endothelial cells and
230 pneumocytes as expected in the lung (Fig. 4a, d). In K18-hACE2 mice, transcriptional changes following infection
231 were relatively modest, with the largest change in gene signatures associated with myeloid cells, classical
232 monocytes, and alveolar macrophages only by 6 dpi (Fig. 4b, c). In contrast, PWK x K18-hACE2 mice
233 demonstrated dynamic changes in the lung, including a marked stromal cell response as well as recruitment of
234 classical monocytes at 3 dpi that was resolving by 6 dpi (Fig. 4e). Evidence of T cell infiltration was also observed
235 at 3 dpi in gene cluster 3 that contained monocytes and endothelial cells (Fig. 4d, f). In contrast, endothelial cell
236 gene expression was reduced in representation at both 3 and 6 dpi compared to naïve lungs. However, this is likely
237 due to increased cellular complexity of the lung at 3dpi, and a greater transcriptional signature of type II
238 pneumocytes by 6 dpi (Fig. 4d) which may indicate cellular proliferation and repair at this time. These results
239 demonstrate an early, orchestrated tissue-level response in PWK x K18-hACE2 mice resulting in coordinated
240 monocyte and T cell infiltration, that was substantially delayed in the K18-hACE2 mouse model.
241
242 Previous studies in C57BL/6 mice have demonstrated a role for IFNAR signaling in immune cell recruitment to the
243 lung, but little to no role in control of SARS-CoV-2 replication or protection from clinical disease [15,16]. From the
244 results obtained thus far, we suspected that low levels of IFN-I expression in K18-hACE2 at early time points
245 enables uncontrolled virus replication but also renders this strain difficult to study the antiviral functions of IFN-I.
246 To explore this further, expression dynamics of ISGs previously demonstrated to have direct anti-viral functions
247 towards SARS-CoV-2[45]were examined. Like the monocyte response in PWK x K18-hACE2 mice, expression of
248 representative ISGs *Ifi205, Zbp1, Ifit3, Ly6e, Gbp3 and Bst2* uniformly peaked at 3 dpi and was resolving by 6 dpi
249 (Fig. 5a). ISG expression changes were generally apparent across all transcriptional clusters, suggesting that no
250 single cell type was uniquely responsible. In contrast, ISG expression in K18-hACE2 mice was not uniformly
251 orchestrated and was generally muted compared to PWK x K18-hACE2 mice. Low levels of *Ifi205, Zbp1 and Gbp3*
252 expression at 3 dpi were further increasing at 6 dpi, whereas increased *Ifit3* and *Bst2* expression at 3 dpi was
253 sustained at 6 dpi, and *Ly6e* expression was not changed over time. The dynamics of ISG expression appeared

254 closely related to virus clearance. By RNAscope analysis for SARS-CoV-2 nucleic acid, virus was similarly
255 distributed throughout lungs of both mouse genotypes at 3 dpi (Fig. 5b). By 6 dpi, virus distribution was unchanged
256 in K18-hACE2 mice, but was almost completely cleared from PWK x K18-hACE2 lungs. Thus, the comparison
257 between these highly sensitive and resistant genetic backgrounds reveals orchestrated IFN-I and monocyte responses
258 are closely associated with control of virus replication.
259
260 The distinct contrasts between K18-hACE2 and PWK x K18-hACE2 mice in ISG signatures, chemokine expression
261 and viral dynamics prompted us to test the role of IFN-I by treating both genetic backgrounds with a single dose of
262 anti-IFNAR neutralizing monoclonal antibody 24 h prior to infection. For these studies, K18-hACE2 and PWK x
263 K18-hACE2 were inoculated with a lethal dose (10^4 pfu of SARS-CoV-2), with male PWK x K18-hACE2
264 maintaining a highly resistant phenotype (Fig. S2a). Consistent with correlation coefficient analysis, neutralization
265 of IFN-I signaling in male mice resulted in reduced expression of most inflammatory cytokines and chemokines in
266 BAL fluid at 3 and 6 dpi regardless of genetic background (Fig. 6a). Exceptions in PWK x K18-hACE2 mice
267 included increased IFNα and IL-12p70 at 3dpi, and no change in IFNγ and IL-18 at 6 dpi. Virus titers in lung of
268 PWK x K18-hACE2 mice were increased by approximately 8-fold at 3dpi, with virus clearance delayed in most
269 mice, increased neuroinvasion, and increased lethality (Fig. 6b-d). In contrast, while neutralization of IFN-I
270 signaling resulted in a 5-fold increase in infectious titers in C57Bl/6 K18-hACE2 lung at 3dpi, it did not change
271 kinetics of virus clearance or rates of survival (Fig. 6d). Thus, early IFN-I expression in PWK x K18-hACE2
272 controls peak virus loads, kinetics of virus clearance and dissemination to tissues outside of the lung. Importantly,
273 this work definitively demonstrates the antiviral role of IFN-I to SARS-CoV-2 in vivo and illustrates the role of host
274 genetics in determining these critical events.
275

276 **DISCUSSION**

277 Although the COVID-19 pandemic has spurred unprecedented analyses of human cohorts, the drivers of
278 dysregulated inflammation and how they relate to virus replication kinetics in tissues are not understood. Thus,
279 animal models that recapitulate the complexities of human COVID-19 virus replication dynamics and inflammatory
280 responses are essential to better understand mechanisms of protection and pathogenesis. Here, we report an
281 expanded range of SARS-CoV-2 disease phenotypes in mice using F1 progeny from the eight CC founder strains, as

282 well as BALB/cJ and DBA/2J, crossed to K18-hACE-2 transgenic mice. The various genetic backgrounds yielded a
283 spectrum of disease phenotypes including severe (C57BL/6J and A/J), severe with sex-bias (CAST/EiJ, NOD/ShiLtJ
284 and WSB/EiJ), and resistant mice exhibiting relatively high pathology but non-lethal disease (PWK/PhJ,
285 NZO/HILtJ, 129S1/SvImJ, DBA/2J and BALB/cJ). Variability in outcomes of SARS-CoV-2 infection in these
286 mouse models was associated with distinct dynamics of innate immunity. Herein, control of virus replication in the
287 lung and host resistance to disease can be independent from the early peak titer, but it was closely associated with a
288 phased amplification and resolution of proinflammatory mediators associated with rapid control of virus replication
289 in lung and prevention of virus dissemination to other organs. These favorable outcomes of COVID-19 are most
290 clearly modeled by examining SARS-CoV-2 infection of PWK and NZO x K18-hACE2. In contrast, infection of
291 C57Bl/6 or A/J x K18-hACE2 represent a model of inefficient IFN expression in the lung, failed host control of
292 virus replication and dysregulated proinflammatory responses[8,10,43,46-48]. Collectively, the CC x K18-hACE-2 panel
293 represents a genetically diverse population and reflect a broader range of host-viral interactions that influence
294 disease outcomes. Importantly, this panel provides much needed tools to further determine the roles of specific cell
295 types and signaling pathways in orchestrating protective versus pathogenic immunity.
296
297 Early events surrounding the production of antiviral IFNs are key determinants in human outcomes of
298 COVID-19, but a mechanistic understanding is lacking. Evidence linking IFN-I responses to dysregulated immunity
299 and disease severity includes genetic lesions in pattern recognition receptor signaling molecules[3], production of anti-
300 IFN autoantibodies[12], and patterns of IFN-I and ISG expression in respiratory tissues[49]. However, these attributes are
301 linked to subsets of patients with severe COVID-19, which leaves open questions regarding how antiviral functions
302 of IFNs are balanced with inflammation and why some people fail to mount effective antiviral responses despite
303 high viral load or high IFN-I expression. The CC x K18-hACE2 mice revealed that IFN-I responses in lungs of K18-
304 hACE2(C57Bl/6J) are relatively low compared to other specific genetic backgrounds, which may explain why
305 ablation of IFN-I signaling was associated with relatively small effects in this model (this study, and[15,16]). In
306 contrast, the PWK x K18-hACE2 infection model represents the outcome where IFN-I is directly linked to control
307 of peak virus loads, magnitude of inflammatory cytokine expression independent of virus burden, regulation of
308 adaptive immunity, virus clearance, and control of virus dissemination to tissues outside of the lung. It is curious
309 then that IFN-I expression was highest in BAL fluid of WSB x K18-hACE2 that had high early virus burden in the

310 lung with delayed clearance similar to mice with low IFN-I expression (C57Bl/6J-K18-hACE2). Thus, by
311 comparison, viral dynamics, and pathology in WSB x K18-hACE2 mice provide a model of high IFN-I driving
312 pathology combined with inefficient antiviral functions, as these mice had some of the highest lung pathology
313 scores. Interestingly, a survey of immune cell populations in CC founder mice demonstrated that unchallenged WSB
314 mice have the highest percentages of plasmacytoid dendritic cells (pDCs)[50,51], critical producers of IFN-I in blood
315 and tissues. It is possible that the cellular origin of IFN-I in lungs of SARS-CoV-2-infected PWK and WSB x K18-
316 hACE2 mice is different, that pDC function in the WSB background is dysregulated as is observed in severe
317 COVID-19 [52], or that high IFN-I expression and resulting pathology or inflammatory cell milieu inhibits adaptive
318 immunity in WSB mice. Further insight will be gained by comprehensively comparing immunological and
319 transcriptional responses of PWK and WSB x K18-hACE2 mice following challenge with SARS-CoV-2.
320 Importantly, virus dissemination to the CNS does not consistently occur in PWK or WSB genetic backgrounds
321 suggesting that these two new models are particularly valuable in understanding immune cell dynamics in the lung
322 and should be explored for their potential to model post-acute events including sequalae of long-COVID.

323

324 The remarkedly different patterns of ISG expression in lungs of K18-hACE2 and PWK x K18-hACE2 mice
325 begins to clarify how IFN-I signaling can fail to be well orchestrated and effective. We examined canonical ISGs
326 with demonstrated antiviral functions towards SARS-CoV-2 (e.g., Bst2/tetherin and ZBP1[45], as well as Gbp proteins
327 that SARS-CoV-2 VOC have specifically evolved resistance to[53]. Prompt and widespread gene expression was
328 tightly associated with efficient control of virus replication in PWK x K18-hACE2 lungs. However, while ISG
329 expression was increased at 3 dpi of K18-hACE2 mice, it failed to effectively control virus replication resulting in
330 further increases in host gene expression. We speculate that this sustained ISG expression in the presence of
331 relatively high virus burden may provide the environment that facilitates virus evolution to escape individual ISGs.
332 As expected, IFN-I was not solely required for control of virus replication in PWK x K18-hACE2 mice as IFNAR
333 blocking experiments did not result in a rebound of virus titers to the same levels as K18-hACE2 or 100% lethality.
334 However, the PWK genetic background will enable experimental models to empirically determine how antiviral
335 mechanisms are coordinated to control replication, including type III IFNs that have been shown to correlate with
336 virus control in humans[49].

337

338 One limitation of the study is the degree of variability observed in the data likely due to the sublethal virus
339 dose used. However, as exemplified in PWK x K18-hACE2, this was an important element of the experimental
340 design because it enabled observation of host resistance by not overwhelming initial host defenses. Another
341 limitation is the use of heterozygous F1 offspring because important phenotypes could be due to either or both
342 parental alleles, making it difficult to map the genetic loci responsible for a given phenotype. However, K18-hACE2
343 mice were used as a common parent for all F1s and therefore, any differences observed in disease outcome is due to
344 genes received from the unique parental strain (CC founders, BALB/cJ or DBA/2).
345
346 In summary, the phenotypes in diverse mice support a role for the innate immune system in determining
347 COVID-19 severity[3,8,46-48] and can be used to address key knowledge gaps, including mechanisms of innate immune
348 control of virus replication, defining events needed for a well-orchestrated inflammatory response independent of
349 early viral burden, molecular mechanisms of sex-dependent disease severity, and longer-term implications for tissue
350 repair[54] and lung function. Taken together, these observations demonstrate that use of host genetic variation in mice
351 can model different outcomes of SARS-CoV-2 infection, addressing a major deficiency in the toolkit required to
352 combat COVID-19.
353
354 **MATERIALS AND METHODS**
355
356 **Ethics statement**
357 Animal study protocols were reviewed and approved by the Institutional Animal Care and Use Committee (IACUC)
358 at Rocky Mountain Laboratories (RML), NIAID, NIH in accordance with the recommendations in the Guide for the
359 Care and Use of Laboratory Animals of the NIH. All animal experiments were performed in an animal biosafety
360 level 3 (ABSL3) research facility at RML. Standard operating procedures for work with infectious SARS-CoV-2
361 and protocols for virus inactivation were approved by the Institutional Biosafety Committee (IBC) and performed
362 under BSL3 conditions.
363
364 **Virus preparation**

365 SARS-CoV-2 (USA_WA1/2020) from University of Texas Medical Branch (Vero passage 4) was propagated on
366 Vero cells cultured in DMEM supplemented with 10% fetal bovine serum, 1 mM L-glutamine, 50U/ml penicillin
367 and 50ug/ml streptomycin. Culture supernatants were collected at 72 hpi, aliquoted and stored at -80ºC.
368

369 **Mice, virus infection, and in vivo block of IFNAR1**

370 CC founder x C57BL/6J -K18-hACE2 F1 were provided by The Jackson Laboratories and include the following:
371 B6.Cg-Tg (K18-ACE2)2PrImn/J), 034860; (A/J x B6.Cg-Tg(K18-ACE2)2Prlmn/J)F1/J, 035940; (PWK/PhJ x
372 B6.Cg-Tg(K18-ACE2)2Prlmn/J)F1/J, 035938; (NZO/HlLtJ x B6.Cg-Tg(K18-ACE2)2Prlmn/J)F1/J, 035936;
373 (129S1/SvImJ x B6.Cg-Tg(K18-ACE2)2Prlmn/J)F1/J, 035934; (CAST/EiJ x B6.Cg-Tg(K18-ACE2)2Prlmn/J)F1/J,
374 035937; (NOD/ShiLtJ x B6.Cg-Tg(K18-ACE2)2Prlmn/J)F1/J, 035935; (WSB/EiJ x B6.Cg-Tg(K18-
375 ACE2)2Prlmn/J)F1/J, 035939; (BALB/cJ x B6.Cg-Tg(K18-ACE2)2Prlmn/J)F1/J, 035941; (DBA/2J x B6.Cg-
376 Tg(K18-ACE2)2Prlmn/J)F1/J 035943. Six- to 12-week-old male and female mice were inoculated by the intranasal
377 route with 10^3 pfu of SARS-CoV-2 in a volume of 50ul PBS (Gibco). Prior to inoculation mice were anesthetized
378 by inhalation of isoflurane. Mice were monitored daily for clinical signs of disease and weight loss. In IFNAR1
379 blocking experiments, male K18-hACE2 and PWK x K18-hACE2 mice were inoculated intraperitoneally anti-
380 IFNAR1 (MAR1-5A3, BioCell) or msIgG1 isotype control (MOPC-21, BioCell) 1 day prior to intranasal
381 inoculation with 10^4 pfu of SARS-CoV-2.
382

383 **Virus titration**

384 Infectious virus in lung and brain tissue was quantified by plaque assay. Tissues were collected in 0.5ml of DMEM
385 containing 2% FBS, 50U/ml penicillin and 50ug/ml streptomycin and immediately frozen. Tissue samples were
386 weighed, and then homogenized using 5mm steel beads and TissueLyzer II high-speed shaker (Qiagen). Ten-fold
387 serial dilutions of homogenates were prepared in duplicate and used to inoculate Vero cells grown in 48-well tissue
388 culture plates. Following 1 hour incubation at 37ºC, the cells were overlayed with 1.5% carboxymethyl cellulose
389 (CMC) in MEM and incubated at 37ºC for 3-4 days. Cells were then fixed in 10%formalin and plaques were
390 visualized by staining with 1% crystal violet diluted in 10% ethanol.
391

392 **Measurement of SARS-CoV-2-specific IgG**

393 Sera were collected at 21 dpi from mice that survived SARS-CoV-2 infection. SARS-CoV-2 spike protein-specific
394 IgG was measured using SARS-CoV2 spike protein serological IgG ELISA kit (Cell Signaling Technology) per
395 manufacturer's instructions.
396
397 **Multiplex cytokine/chemokine analysis**
398 Sera were collected from SARS-CoV-2-infected mice at 3 and 6 dpi by centrifugation of whole blood in GelZ serum
399 separation tubes (Sarstedt). BAL samples were recovered by insufflation of lungs with 1 ml sterile PBS followed by
400 aspiration to collect ~0.5ml volume of fluid. SARS-CoV-2 in sera and BAL fluid was inactivated by using γ-
401 irradiation (2 MRad) and removed from the BSL3 laboratory. Cytokine concentrations in serum and BAL were
402 measured using a 26-Procartaplex mouse cytokine/chemokine panel (ThermoFisher EPX260-26088-901) combined
403 with a Simplex IFN*a* assay (ThermoFisher EPX01A-26027-901). Samples were run on a Luminex Bio-Plex 200
404 system with BioPlex Manager 6.1.1 software. Data represented are from samples collected from individual mice.
405
406 **Histopathology and *in situ* hybridization**
407 Tissues were fixed in 10% neutral buffered formalin for a minimum of 7 days with 2 changes according to IBC-
408 approved standard operating procedure. Tissues were processed with a Sakura VIP-6 Tissue Tek, on a 12-hour
409 automated schedule, using a graded series of ethanol, xylene, and PureAffin. Embedded tissues were sectioned at 5
410 µm and dried overnight at 42°C prior to staining with hematoxylin and eosin. Chromogenic detection of SARS-
411 CoV-2 viral RNA was performed using the RNAscope VS Universal AP assay (Advanced Cell Diagnostics Inc.) on
412 the Ventana Discovery ULTRA stainer using a SARS-CoV-2 specific probe (Advanced Cell Diagnostics Inc. cat.
413 848569). *In situ* hybridization was performed according to manufacturer's instructions. ACE2 immunoreactivity
414 was detected using R&D Systems AF933 at a 1:100 dilution. The secondary antibody is the Vector Laboratories
415 catalog number MP-7405 ImmPress anti-goat polymer. The tissues were then processed for immunohistochemistry
416 using the Discovery Ultra automated stainer (Ventana Medical Systems) with a ChromoMap DAB kit (Roche Tissue
417 Diagnostics cat. 760-159).
418
419 **Visium spatial transcriptomics and processing**

420 Formalin-fixed, paraffin-embedded samples were sectioned directly onto Visium Spatial for FFPE Gene Expression
421 Mouse Transcriptome slides (6.5 X 6.5 mm) and processed for sequencing, according to the manufacturer's
422 procedure (10X Genomics, Pleasanton, CA). Resulting libraries were sequenced as 28/10/10/50 base reads on the
423 NovaSeq instrument using the S2 Reagent kit in paired-end mode (Illumina, San Diego, CA). Fastq files were
424 processed with Spaceranger-1.4.2 pipeline. Processed data were then analyzed on R studio (2021.09.1, Build 372)
425 with Seurat (v4.0)[55]. We trimmed spots with zero count and normalized using SCtransform function[56]. Then data
426 were integrated using IntegrateAnchor method[57]. A total of 2000 highly variable genes identified by the
427 SCtransform function in the Seurat[55]package were used for principal component analysis (PCA)-based
428 dimensionality reduction with RunPCA. Uniform Manifold Approximation and Projection (UMAP) with a
429 resolution of 0.05 was utilized to visualize single-cell clustering using principal components (PCs) 1 to 30.
430

431 **Quantitative real-time PCR**

432 Total lung RNA was extracted from homogenized lysates using the *mir*Vana miRNA Isolation Kit (Invitrogen cat.
433 AM1560) following the manufacturer's protocol for total RNA isolation. Total RNA samples were quantified using
434 a Nanodrop spectrophotometer (Thermo cat. ND-2000C), and reverse transcribed to cDNA using the SuperScript IV
435 VILO Master Mix with ezDNase enzyme (Invitrogen cat. 11766050) following the manufacturer's instructions.
436 Expression of mouse *Ace2*, mouse *Gapdh*, and human ACE2 were quantified by qPCR using the ViiA7 Real-Time
437 PCR System (Thermo cat. 44535545). TaqMan probes targeting mouse *Gapdh* (Thermo probe ID
438 Mm99999915_g1) and human ACE2 (Thermo probe ID Hs01085333_m1) were used in conjunction with the
439 TaqMan Fast Advanced Master Mix (Thermo cat. 4444556) and the ViiA7 Real-Time PCR System with
440 QuantStudio Software (Thermo cat. 44535545). Samples were run in technical triplicate in 10ul reaction volumes on
441 a 384-well plate, and hACE2 transcript abundance values were normalized to m*Gapdh* in each sample and relative
442 expression was calculated using a reference lung sample (K18-hACE2) and the delta delta-Ct method.
443

444 **Statistical analysis**

445 Comparison of survival curves in males versus females for each strain was performed using the log-rank (Mantel-
446 Cox) test. One-way analysis of variance (ANOVA) with Tukey's multiple comparison posttest was used to compare
447 cytokine and chemokine levels of BAL and serum. Differences between groups were considered significant at a *P*

value of <0.05. All statistical analyses were performed with graphPad Prism 8.0 (GraphPad Software) or Qlucore Omics Explorer Version 3.7 (Qlucore AB). Correlation analyses were performed by computing Spearman's coefficients and visualized using ggcorrplot. Correlation tests with $P < 0.001$ were displayed.

Data Availability

All data are available without restrictions. Visium RNA-seq data that support the findings of this study have been deposited in Gene Expression Omnibus (GEO) public database with the accession code XXX.

References

1 Richardson, S. *et al.* Presenting Characteristics, Comorbidities, and Outcomes Among 5700 Patients Hospitalized With COVID-19 in the New York City Area. *JAMA* **323**, 2052-2059, doi:10.1001/jama.2020.6775 (2020).

2 Long, Q. X. *et al.* Clinical and immunological assessment of asymptomatic SARS-CoV-2 infections. *Nat Med* **26**, 1200-1204, doi:10.1038/s41591-020-0965-6 (2020).

3 Zhang, Q. *et al.* Inborn errors of type I IFN immunity in patients with life-threatening COVID-19. *Science* **370**, doi:10.1126/science.abd4570 (2020).

4 Mainous, A. G., Rooks, B. J., Wu, V. & Orlando, F. A. COVID-19 Post-acute Sequelae Among Adults: 12 Month Mortality Risk. *Frontiers in Medicine* **8**, doi:10.3389/fmed.2021.778434 (2021).

5 Docherty, A. B. *et al.* Features of 20 133 UK patients in hospital with covid-19 using the ISARIC WHO Clinical Characterisation Protocol: prospective observational cohort study. *BMJ* **369**, m1985, doi:10.1136/bmj.m1985 (2020).

6 Pairo-Castineira, E. *et al.* Genetic mechanisms of critical illness in COVID-19. *Nature* **591**, 92-98, doi:10.1038/s41586-020-03065-y (2021).

7 Wong, L.-Y. R. & Perlman, S. Immune dysregulation and immunopathology induced by SARS-CoV-2 and related coronaviruses — are we our own worst enemy? *Nature Reviews Immunology* **22**, 47-56, doi:10.1038/s41577-021-00656-2 (2022).

8 Schultze, J. L. & Aschenbrenner, A. C. COVID-19 and the human innate immune system. *Cell* **184**, 1671-1692, doi:10.1016/j.cell.2021.02.029 (2021).

9 Park, A. & Iwasaki, A. Type I and Type III Interferons - Induction, Signaling, Evasion, and Application to Combat COVID-19. *Cell Host Microbe* **27**, 870-878, doi:10.1016/j.chom.2020.05.008 (2020).

10 Lucas, C. *et al.* Longitudinal analyses reveal immunological misfiring in severe COVID-19. *Nature* **584**, 463-469, doi:10.1038/s41586-020-2588-y (2020).

11 Acharya, D., Liu, G. & Gack, M. U. Dysregulation of type I interferon responses in COVID-19. *Nature Reviews Immunology* **20**, 397-398, doi:10.1038/s41577-020-0346-x (2020).

12 Bastard, P. *et al.* Autoantibodies against type I IFNs in patients with life-threatening COVID-19. *Science* **370**, doi:10.1126/science.abd4585 (2020).

13 Hadjadj, J. *et al.* Impaired type I interferon activity and inflammatory responses in severe COVID-19 patients. *Science* **369**, 718-724, doi:10.1126/science.abc6027 (2020).

14 Galani, I. E. *et al.* Untuned antiviral immunity in COVID-19 revealed by temporal type I/III interferon patterns and flu comparison. *Nat Immunol* **22**, 32-40, doi:10.1038/s41590-020-00840-x (2021).

15 Sun, J. *et al.* Generation of a Broadly Useful Model for COVID-19 Pathogenesis, Vaccination, and Treatment. *Cell* **182**, 734-743.e735, doi:10.1016/j.cell.2020.06.010 (2020).

16 Israelow, B. *et al.* Mouse model of SARS-CoV-2 reveals inflammatory role of type I interferon signaling. *J Exp Med* **217**, doi:10.1084/jem.20201241 (2020).

17 Gan, E. S. *et al.* A mouse model of lethal respiratory dysfunction for SARS-CoV-2 infection. *Antiviral Res* **193**, 105138, doi:10.1016/j.antiviral.2021.105138 (2021).
18 Munoz-Fontela, C. *et al.* Animal models for COVID-19. *Nature* **586**, 509-515, doi:10.1038/s41586-020-2787-6 (2020).
19 Winkler, E. S. *et al.* SARS-CoV-2 infection of human ACE2-transgenic mice causes severe lung inflammation and impaired function. *Nat Immunol* **21**, 1327-1335, doi:10.1038/s41590-020-0778-2 (2020).
20 Chen, R. E. *et al.* In vivo monoclonal antibody efficacy against SARS-CoV-2 variant strains. *Nature* **596**, 103-108, doi:10.1038/s41586-021-03720-y (2021).
21 Johnson, B. A. *et al.* Loss of furin cleavage site attenuates SARS-CoV-2 pathogenesis. *Nature* **591**, 293-299, doi:10.1038/s41586-021-03237-4 (2021).
22 VanBlargan, L. *et al.* A potently neutralizing anti-SARS-CoV-2 antibody inhibits variants of concern by binding a highly conserved epitope. *bioRxiv*, doi:10.1101/2021.04.26.441501 (2021).
23 Yinda, C. K. *et al.* K18-hACE2 mice develop respiratory disease resembling severe COVID-19. *PLoS Pathog* **17**, e1009195, doi:10.1371/journal.ppat.1009195 (2021).
24 Zheng, J. *et al.* COVID-19 treatments and pathogenesis including anosmia in K18-hACE2 mice. *Nature* **589**, 603-607, doi:10.1038/s41586-020-2943-z (2021).
25 Roberts, A., Pardo-Manuel de Villena, F., Wang, W., McMillan, L. & Threadgill, D. W. The polymorphism architecture of mouse genetic resources elucidated using genome-wide resequencing data: implications for QTL discovery and systems genetics. *Mamm Genome* **18**, 473-481, doi:10.1007/s00335-007-9045-1 (2007).
26 Srivastava, A. *et al.* Genomes of the Mouse Collaborative Cross. *Genetics* **206**, 537-556, doi:10.1534/genetics.116.198838 (2017).
27 Williamson, E. J. *et al.* Factors associated with COVID-19-related death using OpenSAFELY. *Nature* **584**, 430-436, doi:10.1038/s41586-020-2521-4 (2020).
28 Ashbrook, D. G. *et al.* A platform for experimental precision medicine: The extended BXD mouse family. *Cell Syst* **12**, 235-247 e239, doi:10.1016/j.cels.2020.12.002 (2021).
29 Kumari, P. *et al.* Neuroinvasion and Encephalitis Following Intranasal Inoculation of SARS-CoV-2 in K18-hACE2 Mice. *Viruses* **13**, doi:10.3390/v13010132 (2021).
30 Oladunni, F. S. *et al.* Lethality of SARS-CoV-2 infection in K18 human angiotensin-converting enzyme 2 transgenic mice. *Nat Commun* **11**, 6122, doi:10.1038/s41467-020-19891-7 (2020).
31 Ackermann, M. *et al.* Pulmonary Vascular Endothelialitis, Thrombosis, and Angiogenesis in Covid-19. *N Engl J Med* **383**, 120-128, doi:10.1056/NEJMoa2015432 (2020).
32 Gupta, A. *et al.* Extrapulmonary manifestations of COVID-19. *Nat Med* **26**, 1017-1032, doi:10.1038/s41591-020-0968-3 (2020).
33 Gu, S. X. *et al.* Thrombocytopathy and endotheliopathy: crucial contributors to COVID-19 thromboinflammation. *Nat Rev Cardiol* **18**, 194-209, doi:10.1038/s41569-020-00469-1 (2021).
34 Bernardes, J. P. *et al.* Longitudinal Multi-omics Analyses Identify Responses of Megakaryocytes, Erythroid Cells, and Plasmablasts as Hallmarks of Severe COVID-19. *Immunity* **53**, 1296-1314 e1299, doi:10.1016/j.immuni.2020.11.017 (2020).
35 Schulte-Schrepping, J. *et al.* Severe COVID-19 Is Marked by a Dysregulated Myeloid Cell Compartment. *Cell* **182**, 1419-1440 e1423, doi:10.1016/j.cell.2020.08.001 (2020).
36 Arunachalam, P. S. *et al.* Systems biological assessment of immunity to mild versus severe COVID-19 infection in humans. *Science* **369**, 1210-1220, doi:10.1126/science.abc6261 (2020).
37 Tostanoski, L. H. *et al.* Ad26 vaccine protects against SARS-CoV-2 severe clinical disease in hamsters. *Nat Med* **26**, 1694-1700, doi:10.1038/s41591-020-1070-6 (2020).
38 Chakraborty, S. *et al.* Proinflammatory IgG Fc structures in patients with severe COVID-19. *Nat Immunol* **22**, 67-73, doi:10.1038/s41590-020-00828-7 (2021).
39 Consiglio, C. R. *et al.* The Immunology of Multisystem Inflammatory Syndrome in Children with COVID-19. *Cell* **183**, 968-981 e967, doi:10.1016/j.cell.2020.09.016 (2020).
40 Mathew, D. *et al.* Deep immune profiling of COVID-19 patients reveals distinct immunotypes with therapeutic implications. *Science* **369**, doi:10.1126/science.abc8511 (2020).
41 Shen, B. *et al.* Proteomic and Metabolomic Characterization of COVID-19 Patient Sera. *Cell* **182**, 59-72 e15, doi:10.1016/j.cell.2020.05.032 (2020).
42 Silvin, A. *et al.* Elevated Calprotectin and Abnormal Myeloid Cell Subsets Discriminate Severe from Mild COVID-19. *Cell* **182**, 1401-1418 e1418, doi:10.1016/j.cell.2020.08.002 (2020).

547 43 Takahashi, T. *et al.* Sex differences in immune responses that underlie COVID-19 disease outcomes.
548 *Nature* **588**, 315-320, doi:10.1038/s41586-020-2700-3 (2020).
549 44 Wilk, A. J. *et al.* A single-cell atlas of the peripheral immune response in patients with severe COVID-19.
550 *Nat Med* **26**, 1070-1076, doi:10.1038/s41591-020-0944-y (2020).
551 45 Martin-Sancho, L. *et al.* Functional landscape of SARS-CoV-2 cellular restriction. *Mol Cell* **81**, 2656-
552 2668.e2658, doi:10.1016/j.molcel.2021.04.008 (2021).
553 46 Blanco-Melo, D. *et al.* Imbalanced Host Response to SARS-CoV-2 Drives Development of COVID-19.
554 *Cell* **181**, 1036-1045 e1039, doi:10.1016/j.cell.2020.04.026 (2020).
555 47 Zanoni, I. Interfering with SARS-CoV-2: are interferons friends or foes in COVID-19? *Curr Opin Virol* **50**,
556 119-127, doi:10.1016/j.coviro.2021.08.004 (2021).
557 48 Ziegler, C. G. K. *et al.* Impaired local intrinsic immunity to SARS-CoV-2 infection in severe COVID-19.
558 *Cell* **184**, 4713-4733 e4722, doi:10.1016/j.cell.2021.07.023 (2021).
559 49 Sposito, B. *et al.* The interferon landscape along the respiratory tract impacts the severity of COVID-19.
560 *Cell* **184**, 4953-4968.e4916, doi:10.1016/j.cell.2021.08.016 (2021).
561 50 Phillippi, J. *et al.* Using the emerging Collaborative Cross to probe the immune system. *Genes & Immunity*
562 **15**, 38-46, doi:10.1038/gene.2013.59 (2014).
563 51 Collin, R., Balmer, L., Morahan, G. & Lesage, S. Common Heritable Immunological Variations Revealed
564 in Genetically Diverse Inbred Mouse Strains of the Collaborative Cross. *J Immunol* **202**, 777-786,
565 doi:10.4049/jimmunol.1801247 (2019).
566 52 Saichi, M. *et al.* Single-cell RNA sequencing of blood antigen-presenting cells in severe COVID-19 reveals
567 multi-process defects in antiviral immunity. *Nature Cell Biology* **23**, 538-551, doi:10.1038/s41556-021-
568 00681-2 (2021).
569 53 Mesner, D. *et al.* SARS-CoV-2 evolution influences GBP and IFITM sensitivity. *Proc Natl Acad Sci U S A*
570 **120**, e2212577120, doi:10.1073/pnas.2212577120 (2023).
571 54 Delorey, T. M. *et al.* COVID-19 tissue atlases reveal SARS-CoV-2 pathology and cellular targets. *Nature*
572 **595**, 107-113, doi:10.1038/s41586-021-03570-8 (2021).
573 55 Hao, Y. *et al.* Integrated analysis of multimodal single-cell data. *Cell* **184**, 3573-3587.e3529,
574 doi:10.1016/j.cell.2021.04.048 (2021).
575 56 Hafemeister, C. & Satija, R. Normalization and variance stabilization of single-cell RNA-seq data using
576 regularized negative binomial regression. *Genome Biol* **20**, 296, doi:10.1186/s13059-019-1874-1 (2019).
577 57 Stuart, T. *et al.* Comprehensive Integration of Single-Cell Data. *Cell* **177**, 1888-1902.e1821,
578 doi:10.1016/j.cell.2019.05.031 (2019).
579

580

581 **Supplementary Materials**

582 Fig. S1. Survival, weight loss and SARS-CoV-2 replication kinetics in BALB/cxK18-hACE2 or DBAxK18-hACE2
583 F1 progeny

584 Fig. S2. Survival curve for high dose SARS-COV-2 infection in K18-hACE2 and PWK x K18-hACE2 male and
585 female mice. Relative expression of human *ACE2* in the lungs of naive CCxK18-hACE2 F1 progeny

586 Fig. S3. Examples of pathology in the brain of SARS-CoV-2-infected CCxK18-hACE2 F1 progeny

587 Fig. S4. Heatmaps of interferon, cytokine and chemokine expression in the serum compared to the BAL of SARS-
588 CoV-2-infected CCxK18-hACE2 F1 progeny.

589 Fig. S5. Interferon, cytokine and chemokine expression in the bronchoalveolar lavage from SARS-CoV-2-infected
590 sensitive and resistant CCxK18-hACE2 F1 progeny.

591 Fig. S6. Interferon, cytokine and chemokine expression in the serum of SARS-CoV-2-infected sensitive and
592 resistant CCxK18-hACE2 F1 progeny

593 Fig. S7. Interferon, cytokine and chemokine expression in the bronchoalveolar lavage of male versus female SARS-
594 CoV-2-infected CCxK18-hACE2 F1 progeny with sex bias (CAST, NOD and WSB).

595 Table S1. Summary of percent survival, weight loss, virus burden and BAL cytokine profiles in K18-hACE2 x CC
596 Founder F1 progeny.

Table S2. Summary of statistical analyses of cytokine and chemokine expression in BAL fluid collected from resistant and sensitive K18-hACE2 x CC Founder F1 progeny.

Table S3. Summary of statistical analyses of cytokine and chemokine expression in BAL fluid collected from resistant PWK x K18-hACE2 and sensitive K18-hACE2 mice.

Acknowledgments:

This work was funded by the Division of Intramural Research, National Institutes of Health, National Institute of Allergy and Infectious Diseases. Thank you to the animal caretaker staff at campuses of both RML and The Jackson Laboratory for their work in animal husbandry.

Author contributions: Each author's contribution to the paper should be listed [we encourage you to follow the CRediT model]. Each CRediT role should have its own line, and there should not be any punctuation in the initials.

Conceptualization: SB, NR, and SMH
Methodology: SJR, NR, SB, and CM
Investigation: SJR, OB, KLM, CS, CC, ML, RMB, AIC, JGS, GLS, RR, SLA, EF, CP, CNB, CP, CB, SM, DPB, JBL, JML, AS, PG, DES, and JS
Visualization: SJR, CNB, JH, DES, CM, DPB, JBL JML, AS, PG, and JS
Funding acquisition: SB and NR
Supervision: SB and NR
Writing – original draft: SB, SJR, CB, AS, NR
Writing – review & editing: SB, SJR, CB, NR

Competing interests:

The authors have no competing interests to declare.

Figure Legends:

Figure 1: CC x K18-hACE2 mice demonstrate a range of clinical severity following infection with SARS-CoV-2. Mice were infected intranasally with 10^3 pfu of SARS-CoV-2 and monitored for survival and weight loss. CC x K18-hACE2 were classified as: (**a)** sensitive with 50% or greater mortality and no difference between males and females, **(b)** resistant with 35% or less mortality, or **(c)** sensitive with a sex bias as having statistically significant difference between sensitivity of male and female mice. Infection was confirmed in all surviving mice by

632 seroconversion toSARS-CoV-2 nucleoprotein (N=6-8/per sex). Graphs of percent starting weight show the mean ±
633 SD.
634
635 **Figure 2: Virus replication kinetics and pathology in CC x K18-hACE2.** (**a)** Virus titers (pfu/g tissue) in lung
636 and brain of male and female mice were measured at 3 and 6 dpi. (**b)** H&E staining and *in-situ* hybridization for
637 SARS-CoV-2 nucleic acid predominantly localizing to pneumocytes in areas of lung inflammation. Serial sections
638 demonstrate pathology (upper) and viral RNA distribution (lower; Red). Scale bars represent 100 μm. (**c)** Examples
639 of pathology scoring from H&E-stained lung sections. Scale bars represent 500 μm. (**d),** Lung pathology scores for
640 CC Founder F1 males and females at 3 and 6 dpi. N = 6/time point/sex. Violin plots show all data points **(a, d)**
641
642 **Figure 3: Timing of IFN-I and inflammatory cytokine responses in the lung is associated with clinical severity**
643 **in CC x K18-hACE2.** (**a)** Box plots of IFNα protein in BAL from CC x K18-hACE2 mice at 3 dpi. IFNα protein
644 in BAL from **(b)** male and **(c)** female resistant (PWK, NZO and 129S1 x K18-hACE2) and sensitive (K18-hACE2
645 and A/J x K18-hACE2) mice at 3 and 6 dpi. **(d)** Heatmap of cytokine and chemokine responses in BAL. **(e)** Box
646 plots of quantification of resolving group A cytokines in F1 progeny resistant to lethality (IL-6, IL-27, CCL2,
647 CXCL10), or increasing group B cytokines in sensitive F1 progeny (IL-10, CCL4). IFNα and cytokine correlation
648 plots for K18-hACE2 and PWK x K18-hACE2 at **(f)** 3 dpi and **(g)** 6 dpi. Box plots (drawn in Qlucore software)
649 show individual data points with the box representing the first and third quartiles.
650
651 **Figure 4: Spatial transcriptomics reveals differential innate immune signaling responses of pneumocytes,**
652 **endothelial cells and monocytes in K18-hACE2 and PWK x K18-hACE2 mice.** 10x Genomics Visium spatial
653 transcriptomic analysis of lung sections from K18-hACE2 and PWK x K18-hACE2 at 0 (naïve), 3 and 6 dpi
654 following SARS-CoV-2 inoculation. **(a, d)** Confidence scores for cell type annotations based on unsupervised
655 cluster analysis in K18-hACE2 **(a)** and PWK x K18-hACE2 **(d)**. **(b, e)** Bar graph of cell annotations scores in K18-
656 hACE2 **(b)** and PWK x K18-hACE2 **(e)**. **(c, f)** UMAP representation of identified transcriptional clusters in K18-
657 hACE2 **(c)** and PWK x K18-hACE2 **(f)**.
658

659 **Figure 5: Rapid kinetics of ISG expression associated with virus clearance in PWK x K18-hACE2. (a)**
660 Expression levels of individual ISGs identified in Visium spatial transcriptomics analysis. **(b)** *In-situ* hybridization
661 for SARS-CoV-2 nucleic acid in lung from K18-hACE2 and PWK x K18-hACE2 mice at 3 and 6 dpi. Scale bars
662 represent 1000 μm; scale bars in insets represent 50 μm.
663
664 **Figure 6: Type I IFN signaling controls early SARS-CoV-2 replication and coordinates inflammatory**
665 **responses in PWK x K18-hACE2 mice.** Male K18-hACE2 and PWK x K18-hACE2 mice were treated with anti-
666 IFNAR or msIgG1 isotype control 1 day prior to intranasal inoculation with 10^4 pfu of SARS-CoV-2. **(a)** Heatmap
667 of cytokine and chemokine levels in BAL collected at 3 and 6 dpi. N=5/timepoint/experimental group. Virus titers
668 (pfu/g tissue) in lung **(b)** and brain **(c)** at 3 and 6 dpi **(d).** Percent survival of mice followed daily until 21 dpi. N=10-
669 15/experimental group.
670
671 **Supplemental Figure 1: Survival, weight loss and SARS-CoV-2 replication kinetics in BALB/cJ x K18-hACE2**
672 **or DBA/2J x K18-hACE2 F1 progeny.** (**a)** Survival and weight loss in BALB/cJ x K18-hACE2. (**b)** Survival and
673 weight loss in DBA/2Jx K18-hACE2. (**c)** Virus titers (pfu/g tissue) in lung and brain of male and female mice were
674 measured at 3 and 6 dpi. (**d**) IFNα protein in BAL from BALB/cJ and DBA/2J x K18-hACE2 mice at 3 dpi. **(e)**
675 Heatmap of cytokine expression in BAL.
676
677 **Supplemental Figure 2: Expression of ACE2 in lungs of CC x K18-hACE2 F1 progeny. (a)** Survival curve of
678 K18-hACE2 and PWK x K18-hACE2 male and female mice inoculated intranasally with 10^4 pfu of SARS-CoV-2
679 and monitored for survival**. (b)** Gene expression specific for *hACE2* was measured by real-time RT-PCR and
680 expressed relative to that in male and female K18-hACE2 (C57BL/6J) mice. (**c)** IHC staining for ACE2 in K18-
681 hACE2 and PWK x K18-hACE2 mice. Scale bars represent 50 μm (400X); 200 μm (100X).
682
683 **Supplemental Figure 3: Examples of pathology in the brain of SARS-CoV-2-infected CC x K18-hACE2 F1**
684 **progeny.** (**a)** Small focal areas of inflammation were commonly observed irrespective of genetic strain (circled).
685 Scale bar = 1000 μm. (**b)** increased magnification of (A) demonstrating perivascular cuffing, gliosis, and evidence
686 of necrotic cells in areas of focal inflammation. Scale bar = 200 μm. (**c)** Example of a pronounced lymphocytic

687 inflammatory response with perivascular cuffing and increased cellularity (arrowheads). Scale bar = 100 μm. **(d)**
688 Microthrombus occluding cerebral capillaries and hemorrhage (arrow) observed in CASTxK18-hACE2. Scale bar =
689 100 μm. (**e**) Example of extensive hemorrhage in the brain of CASTxK18-hACE2 F1 progeny associated with
690 extensive virus replication as demonstrated in F. Scale bar = 1000 μm. (**f**) serial section relative to **(e)** showing
691 extensive SARS-CoV-2 genome by RNAscope. Scale bar = 1000 μm. **(g)** Incidence of encephalitis for CC Founder
692 F1 males and females at 3 and 6 dpi scored as absent or present.
693
694 **Supplemental Figure 4: Interferon, cytokine and chemokine expression in the serum compared to the BAL of**
695 **SARS-CoV-2-infected CC x K18-hACE2 F1 progeny.** Heatmap showing relative cytokine levels, as measured by
696 multiplex cytokine assays, for all eight at CCxK18-hACE2 F1s at (**a**) 3 dpi, and **(b)** 6 dpi, and **(c)** for strains with a
697 sex-bias at 3 and 6 dpi.
698
699 **Supplemental Figure 5: Interferon, cytokine, and chemokine expression in the BAL from SARS-CoV-2-**
700 **infected sensitive and resistant CC x K18-hACE2 F1 progeny.** Cytokines were measured at 3 and 6 dpi by
701 multiplex cytokine assays. Box plots represent data from male and female sensitive (K18-hACE2 and A/J x K18-
702 hACE2) and resistant (PWK, NZO and 129S1J x K18-hACE2) F1s. **(a)** "Group A" cytokines with higher production
703 in resistant F1 progeny compared to sensitive F1 progeny at 3 dpi. **(b)** "Group B" cytokines with delayed and
704 sustained production in sensitive compared to resistant F1 progeny. The average cytokine expression in BAL of
705 naïve mice is indicated by a grey dashed line. Box plots (drawn in Qlucore software) show individual data points
706 with the box representing the first and third quartiles.
707
708 **Supplemental Figure 6: Interferon, cytokine, and chemokine expression in the serum from SARS-CoV-2-**
709 **infected sensitive and resistant CCxK18-hACE2 F1 progeny.** Cytokines were measured at 3 and 6 dpi by
710 multiplex cytokine assays. Box plots represent data from male and female sensitive (K18-hACE2 and A/J x K18-
711 hACE2) and resistant (PWK, NZO and 129S1J x K18-hACE2) F1s. **(a)** "Group A" cytokines with higher production
712 in resistant F1 progeny compared to sensitive F1 progeny at 3 dpi. The average cytokine expression in serum of
713 naïve mice is indicated by a grey dashed line. Box plots (drawn in Qlucore software) show individual data points
714 with the box representing the first and third quartiles.

715

716 **Supplemental Figure 7: Interferon, cytokine, and chemokine expression in the BAL from SARS-CoV-2-**
717 **infected CCxK18-hACE2 F1 with a sex bias.** Box plots show cytokine levels in male versus female for CAST,
718 NOD, and WSB x K18-hACE2 F1. Cytokines were measured at 3 and 6 dpi by multiplex cytokine assays. The
719 average cytokine expression in BAL of naïve mice is indicated by a grey dashed line. Box plots (drawn in Qlucore
720 software) show individual data points with the box representing the first and third quartiles.

Table S1. Summary of percent survival, weight loss, virus burden and BAL cytokine profiles in K18-hACE2 x CC Founder F1 progeny.

Table S1

				Peak weight loss		Average Virus Titers in Lung		Cytokine profile BAL	
Strain (F1)	Sex	%Survival	Mean time to death (days)	%	DPI	3 dpi Mean (Std Dev)	6 dpi Mean (Std Dev)	3 dpi	6 dpi
C57Bl/6 x K18-hACE2	M	14	6	16.7	7	1.3e6 (1.8e6)	7.6e4 (1.3e5)	No/Low	High Group A and Group B
	F	29	7	12.0	7	1.5e6 (1.4e6)	8.2e3 (5.7e3)		
A/J x K18-hACE2	M	33	8	15.0	7	2.8e6 (2.2e6)	3.5e4 (6.1e4)	No/Low	High Group A and Group B
	F	66	UD	6.1	7	2.8e6 (2.6e6)	2.7e4 (2.8e4)		
PWK x K18-hACE2	M	83	UD	-	-	1.6e5 (2.3e5)	BLD	High Group A	Moderate Group A and Group B
	F	83	UD	7.0	7	9.2e4 (1.1e4)	BLD		
NZO x K18-hACE2	M	86	UD	13.9	9	2.2e6 (2.8e6)	3.8e3 (3.7e3)	High Group A	High Group A and B
	F	71	UD	21.9	9	1.4e6 (1.2e6)	1.3e3 (1.0e3)		
129S1 x K18-ACE2	M	86	UD	11.8	7	1.3e6 (7.8e5)	3.0e3 (2.8e3)	High Group A	High Group A and Group B
	F	71	UD	12.0	7	8.1e5 (6.4e4)	2.4e4 (4.0e4)		
CAST/EiJ x K18-ACE2	M	0	6	17.2	7	6.7e6 (7.1e6)	4.2e5(3.5e5)	Low Group A	Low Group A
	F	50	15.5	35.8	8	1.6e6(1.4e6)	3.4e4 (2.9e4)	Low Group A	Low Group A
NOD x K18-ACE2	M	33	6.5	6.0	6	2.5e6 (4.4e6)	4.8e3 (5.3e3)	No/Low	Moderate I and II
	F	83	UD	-	-	5.1e5 (7.9e5)	6.4e3 (8.1e3)	No/Low	Moderate I and II
WSB x K18-ACE2	M	66	UD	32.0	11	4.1e6 (1.8e6)	3.1e4 (1.6e4)	Moderate Group A	High Group A and B
	F	0	8	25.1	8	4.4e6 (4.1e6)	2.5e4 (1.2e4)	Moderate Group A	Moderate Group A and Group B
BALB/c x K18-ACE2	M	100	UD	3.0	5	6.0e5 (5.5e5)	1.6e4 (1.3e4)	No/Low	Low Group B
	F	66	UD	8.3	6	3.7e5 (4.2e5)	6.0e2 (1.2e3)	High Group A	High Group A and Group B
DBA/2 x K18-ACE2	M	57	UD	16.0	10	1.5e6 (1.7e6)	1.7e4 (2.2e4)	No/Low	No/Low
	F	71	UD	3.6	6	1.7e6 (1.2e6)	1.2e3 (1.0e3)	No/Low	High Group A and Group B

UD: undetermined
BLD: below limit of detection

742 **Table S2.** Summary of statistical analyses of cytokine and chemokine expression in BAL fluid collected from

743 resistant and sensitive K18-hACE2 x CC Founder F1 progeny.

744 **Table S2.**

	Resistant[1] versus Sensitive[2]		**Kinetics**	
	R>S[3]	S>R[4]	**3 dpi versus 6 dpi[5]**	
	3 dpi	**6 dpi**	**Resistant[1]**	**Sensitive[2]**
Analyte	**P value**	**P value**	**P value**	**P value**
GM-CSF	8.7e-02	2.4e-01	2.4e-01	**1.3e-03**
IFNalpha	**2.9e-05**	1.8e-01	**1.4e-12**	**7.1e-04**
IFNgamma	**1.1e-03**	5.1e-01	**1.9e-05**	**1.3e-03**
IL1-beta	**2.2e-02**	4.1e-01	**1.7e-02**	**1.3e-03**
IL-12p70	**2.1e-03**	1.0e-01	1.0e-00	**1.2e-02**
IL-13	**1.7e-03**	4.6e-01	**1.2e-03**	**2.2e-04**
IL-18	**1.7e-03**	4.7e-01	**1.2e-04**	**1.2e-04**
IL-2	6.4e-01	6.4e-01	**2.5e-03**	**8.8e-04**
IL-4	5.1e-02	5.2e-01	**7.5e-03**	**1.2e-03**
IL-5	8.8e-01	8.8e-01	**5.7e-03**	**4.2e-03**
IL-6	**1.0e-02**	2.4e-01	**7.7e-06**	8.6e-01
TNFα	**3.9e-03**	2.0e-01	9.1e-02	**2.2e-03**
IL-10	6.7e-01	**1.9e-02**	**1.2e-06**	**1.2e-03**
*IL-17A	**1.7e-02**	5.8e-01	**1.7e-02**	6.8e-01
IL-22	**8.3e-03**	1.0e-01	7.9e-01	5.2e-02
IL-23	8.1e-01	9.4e-01	3.2e-01	3.8e-01
IL-27	**2.9e-03**	8.2e-01	**4.1e-02**	4.7e-01
*IL-9	1.0e-00	1.0e-01	4.6e-01	5.1e-01
Eotaxin	**2.0e-02**	7.2e-01	**3.9e-03**	**7.8e-04**
Gro-alpha/KC	**3.0e-03**	2.1e-01	7.9e-01	1.5e-01
CCL2 (MCP1)	**2.5e-03**	6.1e-01	5.5e-02	1.3e-01
CCL3 (MIP1a)	**2.4e-02**	3.1e-01	5.7e-01	**4.8e-04**
CCL4 (MIP1b)	**1.1e-03**	**4.1e-02**	3.0e-01	**1.1e-03**
CCL5 (RANTES)	7.9e-02	6.2e-01	1.3e-01	**3.7e-03**
CCL7 (MCP3)	**1.5e-02**	8.6e-01	9.3e-01	**4.5e-03**
CXCL2 (MIP2a)	**3.7e-03**	4.2e-01	5.8e-02	6.6e-02
CXCL10 (IP10)	**6.4e-03**	6.3e-01	**6.4e-03**	3.4e-01

745 *At or below the lower limit of detection
746 [1] Resistant mice include PWK, NZO and 129S1 x K18-hACE2 F1 progeny
747 [2] Sensitive mice include K18-hACE2 and A/J x K18-hACE2 F1 progeny
748 [3] Higher levels of analytes in resistant compared to sensitive
749 [4] Higher levels of analytes in sensitive compared to resistant
750 [5] Bold black text indicates statistically significant increase from 3 dpi to 6 dpi. Bold blue text
751 indicates statistically significant decrease from 3 dpi to 6 dpi.

752 **Table S3.** Summary of statistical analyses of cytokine and chemokine expression in BAL fluid comparing male and

753 female resistant PWK x K18-hACE2 and sensitive K18-hACE2 x CC Founder F1 progeny.

754 Table S3.

	PWK[1] vs B6[2]	PWK vs B6	PWK vs B6	PWK vs B6
	Females		**Males**	
	3 dpi	**6 dpi**	**3 dpi**	**6 dpi**
Analyte	**P value**	**P value**	**P value**	**P value**
GM-CSF	**9.8e-04**	**8.1e-04**	3.4e-01	1.1e-01
IFNalpha	**6.4e-03**	ND	**3.3e-06**	ND
IFNgamma	**5.2e-04**	1.9e-01	**2.8e-03**	3.3e-01
IL1-beta	**6.0e-04**	**4.9e-03**	1.2e-01	2.0e-01
IL-12p70	6.1e-02	**4.9e-02**	**2.7e-03**	4.4e-01
IL-13	**8.9e-06**	**9.8e-03**	9.7e-02	2.4e-01
IL-18	**1.1e-04**	**8.0e-03**	**3.3e-02**	2.0e-01
IL-2	9.7e-02	9.8e-02	9.0e-01	3.1e-01
IL-4	**1.9e-03**	**3.0e-03**	4.1e-01	1.3e-01
IL-5	1.2e-01	**9.6e-03**	9.5e-01	1.6e-01
IL-6	**4.8e-02**	**4.8e-02**	**3.8e-03**	4.4e-01
TNFα	**4.3e-02**	**1.2e-03**	5.4e-02	2.3e-01
IL-10	**5.3e-03**	**2.9e-03**	6.4e-01	1.9e-01
*IL-17A	**2.3e-03**	**1.6e-02**	4.1e-01	6.8e-01
IL-22	**5.2e-03**	9.7e-01	**1.1e-02**	5.2e-01
IL-23	2.1e-01	2.2e-01	3.0e-01	**5.3e-03**
IL-27	6.6e-01	9.7e-01	**8.0e-04**	4.0e-01
*IL-9	7.4e-01	ND	2.2e01	ND
Eotaxin	5.4e-01	**1.3e-03**	8.5e-02	2.0e-01
Gro-alpha/KC	**7.2e-03**	**1.8e-05**	**2.2e-03**	7.6e-02
CCL2 (MCP1)	6.1e-02	**1.4e-02**	**2.2e-03**	3.2e-01
CCL3 (MIP1a)	4.9e-01	**1.8e-02**	**9.8e-03**	7.6e-02
CCL4 (MIP1b)	**6.7e-03**	**1.0e-06**	**1.9e-03**	5.6e-02
CCL5 (RANTES)	8.6e-01	**1.8e-02**	6.0e-02	3.1e-01
CCL7 (MCP3)	**1.3e-02**	**6.5e-03**	8.0e-02	**3.0e-02**
CXCL2 (MIP2a)	**3.6e-03**	1.2e-01	**4.3e-02**	**2.8e-02**
CXCL10 (IP10)	**1.2e-04**	4.9e-01	**3.2e-02**	**7.2e-03**

755 *At or below the lower limit of detection
756 [1] Resistant mice include PWK x K18-hACE2 F1 progeny
757 [2] Sensitive mice include K18-hACE2 (C57Bl/6J (B6) background)
758 Bold black text indicates statistically significance for higher production in PWK than B6.
759 Bold blue text indicates statistically significance for lower production in PWK than B6.
760
761
762
763

a Sensitive

K18-hACE2 (C57BL/6J)

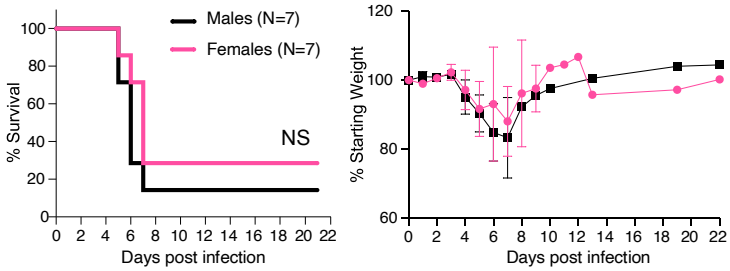

A/JxK18-hACE2

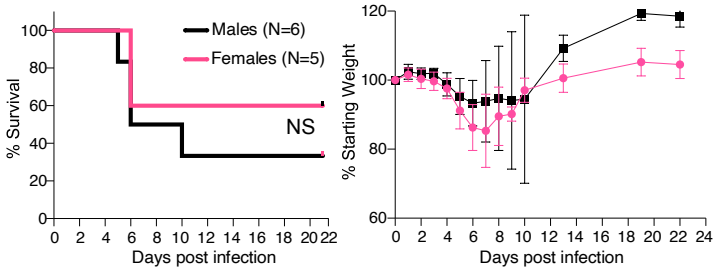

b Resistant

PWKxK18-hACE2

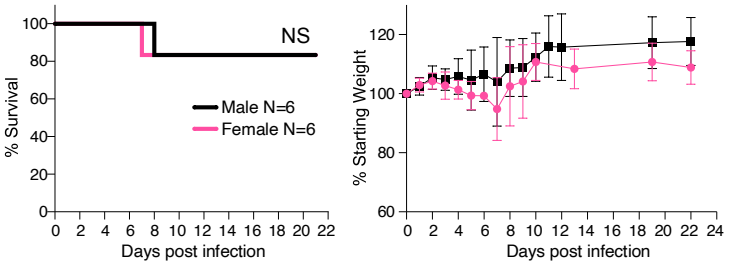

NZOxK18-hACE2

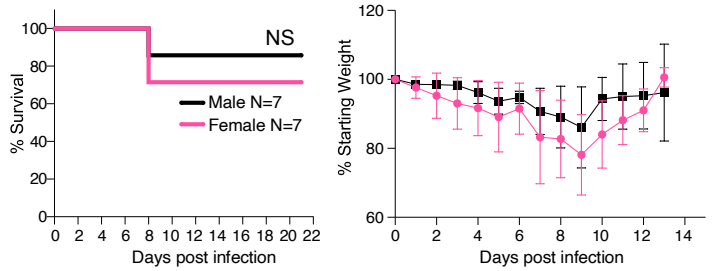

129S1xK18-hACE2

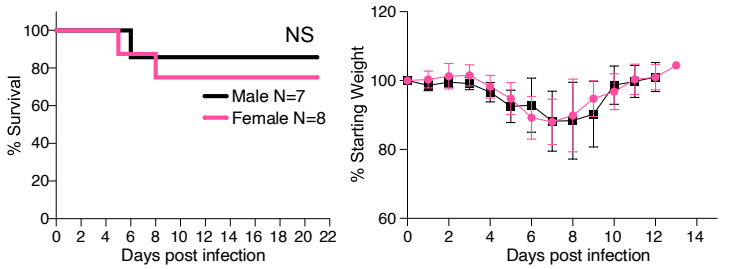

c Sensitive with Sex Bias

CASTxK18-hACE2

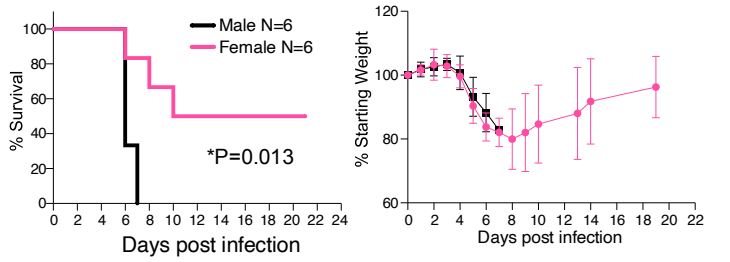

NODxK18-hACE2

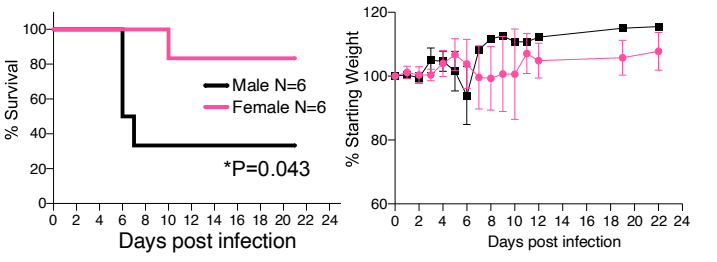

WSBxK18-hACE2

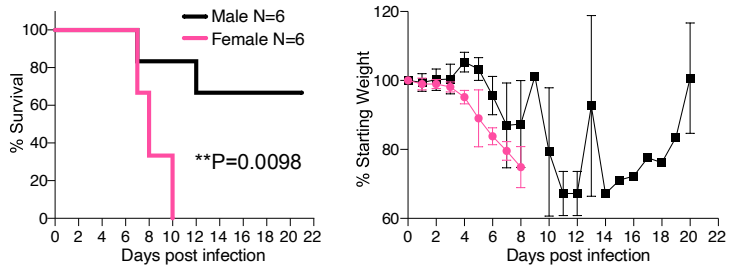

Figure 1

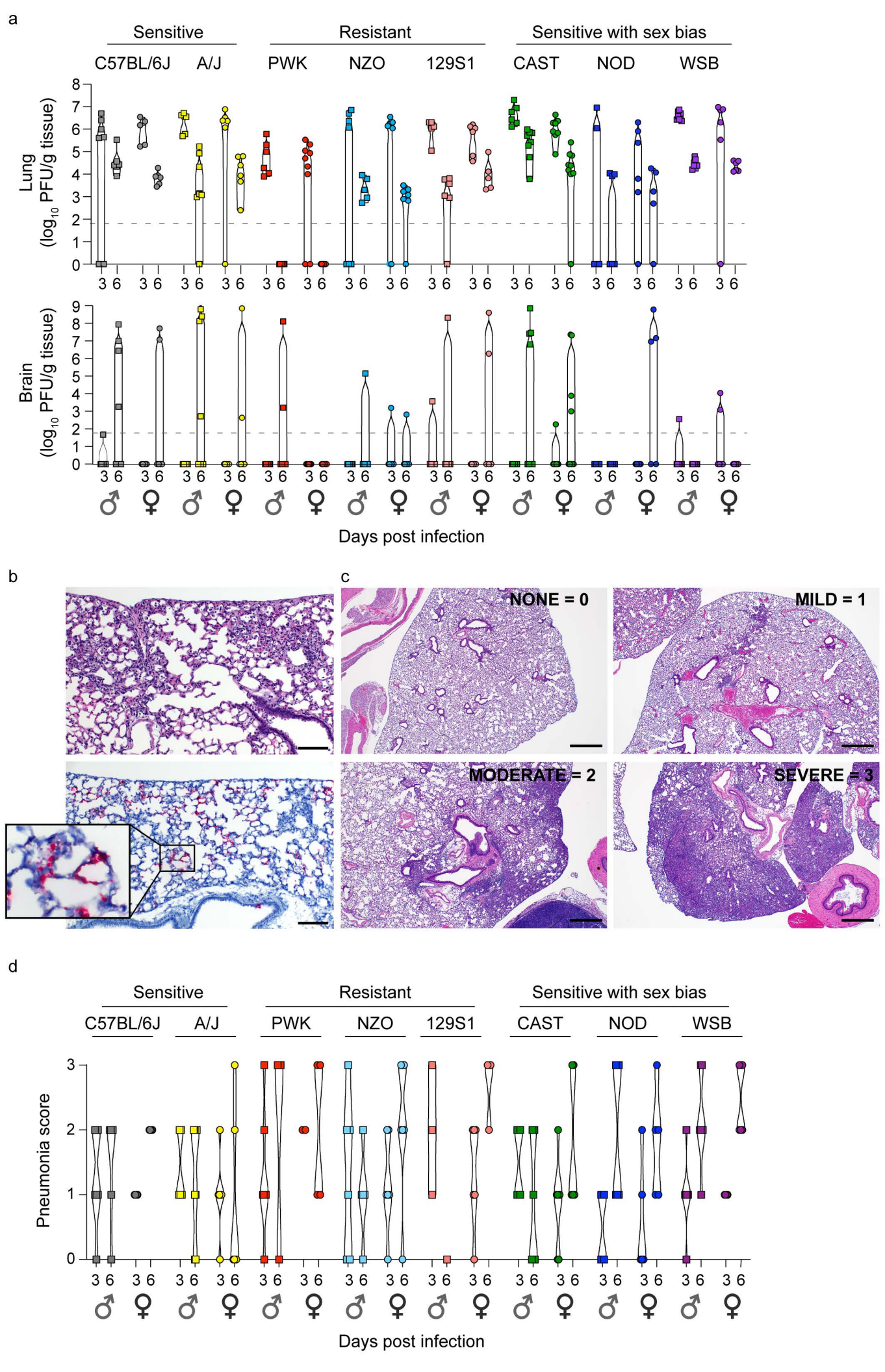
a
Sensitive
Resistant
Sensitive with sex bias
C57BL/6J
A/J
PWK
NZO
129S1
CAST
NOD
WSB
Lung
(log10 PFU/g tissue)
Brain
(log10 PFU/g tissue)
Days post infection
b
c
NONE = 0
MILD = 1
MODERATE = 2
SEVERE = 3
d
Pneumonia score
Days post infection

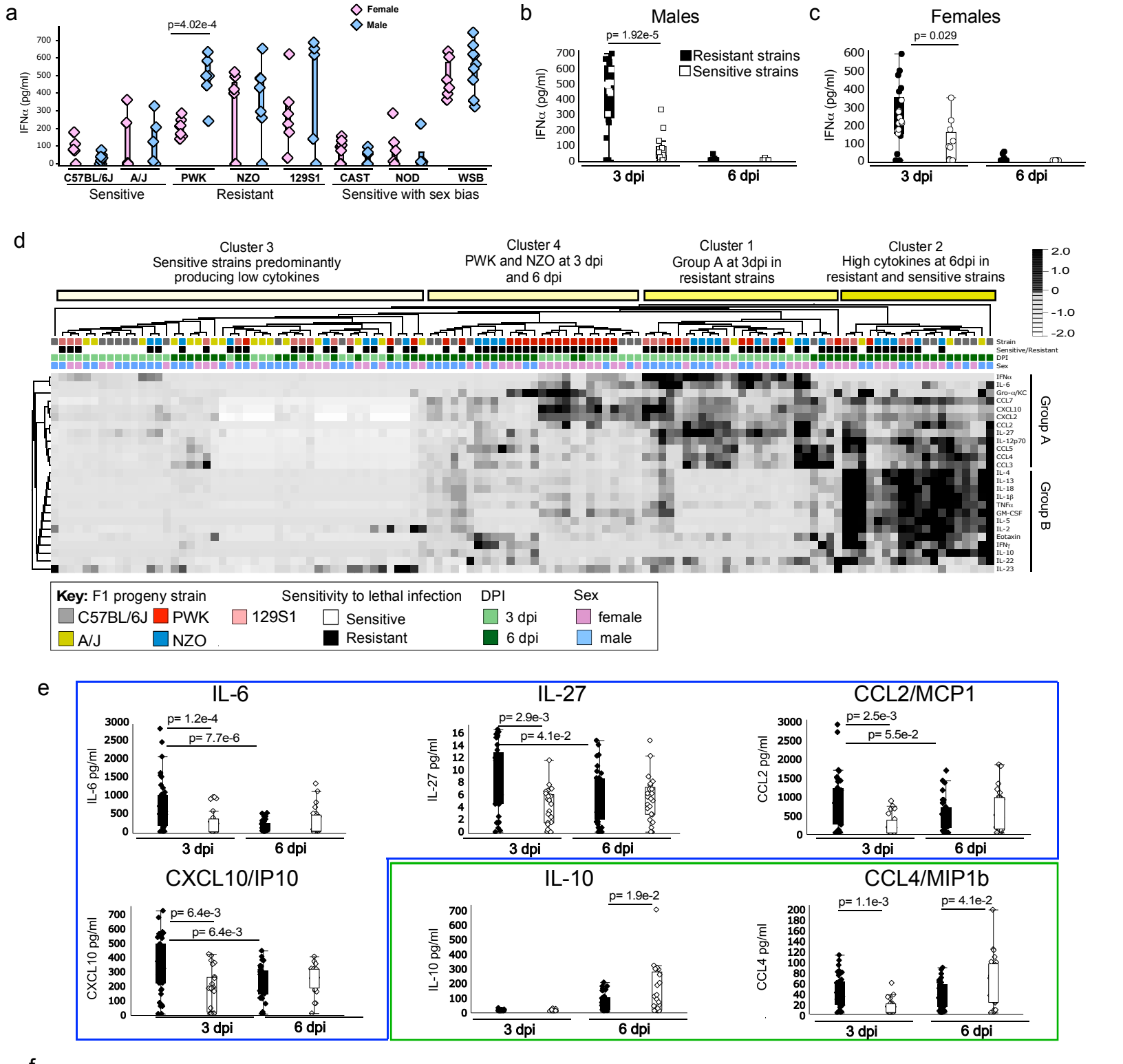
a
Female
Male
p=4.02e-4
IFNα (pg/ml)
C57BL/6J
A/J
PWK
NZO
129S1
CAST
NOD
WSB
Sensitive
Resistant
Sensitive with sex bias
b
Males
p= 1.92e-5
Resistant strains
Sensitive strains
3 dpi
6 dpi
c
Females
p= 0.029
d
Cluster 3
Sensitive strains predominantly producing low cytokines
Cluster 4
PWK and NZO at 3 dpi and 6 dpi
Cluster 1
Group A at 3dpi in resistant strains
Cluster 2
High cytokines at 6dpi in resistant and sensitive strains
Strain
Sensitive/Resistant
DPI
Sex
Group A
Group B
Key: F1 progeny strain
C57BL/6J
PWK
129S1
A/J
NZO
Sensitivity to lethal infection
Sensitive
Resistant
DPI
3 dpi
6 dpi
Sex
female
male
e
IL-6
p= 1.2e-4
p= 7.7e-6
IL-6 pg/ml
IL-27
p= 2.9e-3
p= 4.1e-2
IL-27 pg/ml
CCL2/MCP1
p= 2.5e-3
p= 5.5e-2
CCL2 pg/ml
CXCL10/IP10
p= 6.4e-3
p= 6.4e-3
CXCL10 pg/ml
IL-10
p= 1.9e-2
IL-10 pg/ml
CCL4/MIP1b
p= 1.1e-3
p= 4.1e-2
CCL4 pg/ml
f
K18–hACE2 (C57BL/6J) 3 DPI
PWKxK18–hACE2 3 DPI
g
K18–hACE2 (C57BL/6J) 6 DPI
PWKxK18–hACE2 6 DPI
value

Figure 3

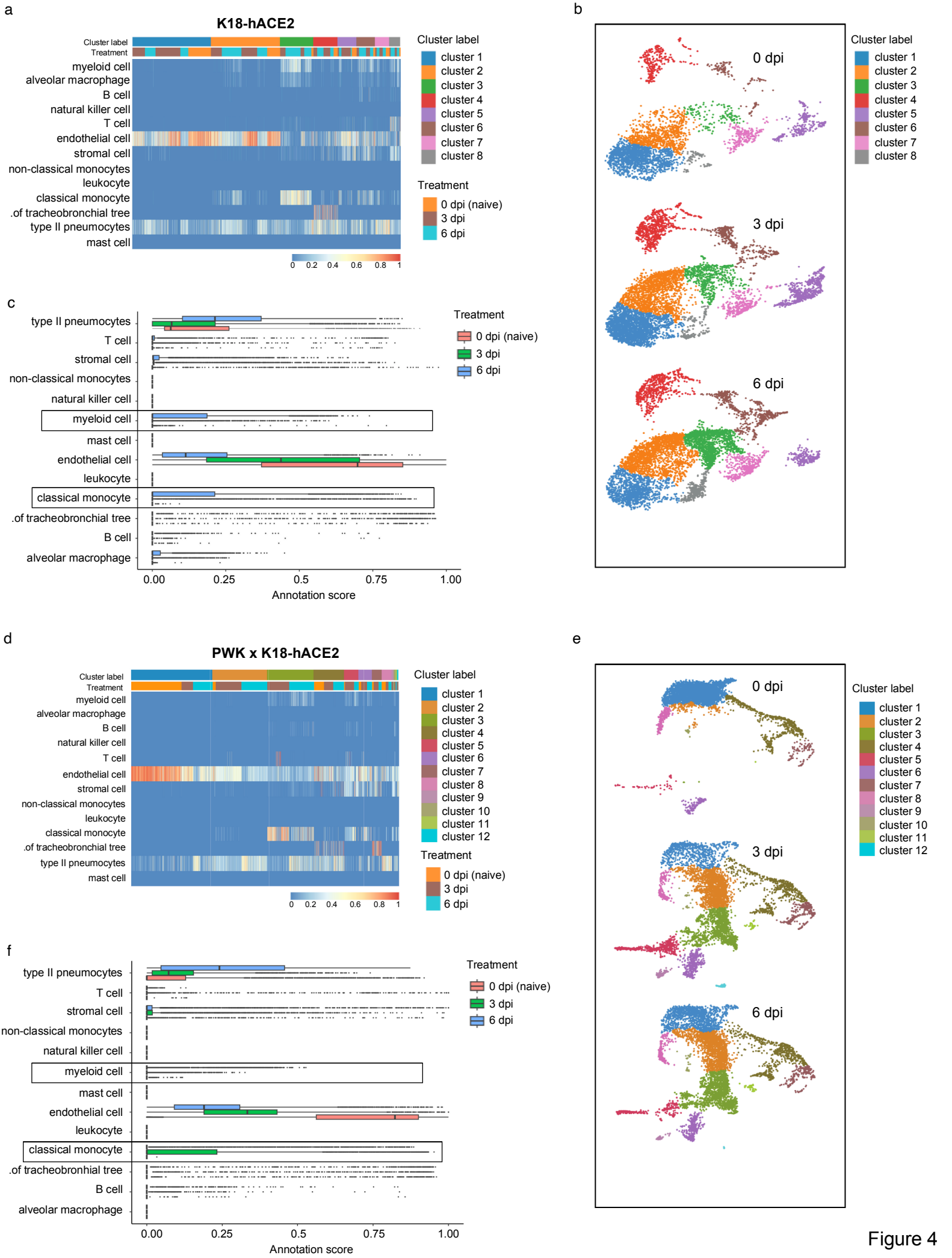
a
K18-hACE2
Cluster label
Treatment
myeloid cell
alveolar macrophage
B cell
natural killer cell
T cell
endothelial cell
stromal cell
non-classical monocytes
leukocyte
classical monocyte
.of tracheobronchial tree
type II pneumocytes
mast cell
0 0.2 0.4 0.6 0.8 1
Cluster label
cluster 1
cluster 2
cluster 3
cluster 4
cluster 5
cluster 6
cluster 7
cluster 8
Treatment
0 dpi (naive)
3 dpi
6 dpi
b
0 dpi
3 dpi
6 dpi
Cluster label
cluster 1
cluster 2
cluster 3
cluster 4
cluster 5
cluster 6
cluster 7
cluster 8
c
type II pneumocytes
T cell
stromal cell
non-classical monocytes
natural killer cell
myeloid cell
mast cell
endothelial cell
leukocyte
classical monocyte
.of tracheobronchial tree
B cell
alveolar macrophage
0.00 0.25 0.5 0.75 1.00
Annotation score
Treatment
0 dpi (naive)
3 dpi
6 dpi
d
PWK x K18-hACE2
Cluster label
Treatment
myeloid cell
alveolar macrophage
B cell
natural killer cell
T cell
endothelial cell
stromal cell
non-classical monocytes
leukocyte
classical monocyte
.of tracheobronchial tree
type II pneumocytes
mast cell
0 0.2 0.4 0.6 0.8 1
Cluster label
cluster 1
cluster 2
cluster 3
cluster 4
cluster 5
cluster 6
cluster 7
cluster 8
cluster 9
cluster 10
cluster 11
cluster 12
Treatment
0 dpi (naive)
3 dpi
6 dpi
e
0 dpi
3 dpi
6 dpi
Cluster label
cluster 1
cluster 2
cluster 3
cluster 4
cluster 5
cluster 6
cluster 7
cluster 8
cluster 9
cluster 10
cluster 11
cluster 12
f
type II pneumocytes
T cell
stromal cell
non-classical monocytes
natural killer cell
myeloid cell
mast cell
endothelial cell
leukocyte
classical monocyte
.of tracheobronhial tree
B cell
alveolar macrophage
0.00 0.25 0.5 0.75 1.00
Annotation score
Treatment
0 dpi (naive)
3 dpi
6 dpi

Figure 4

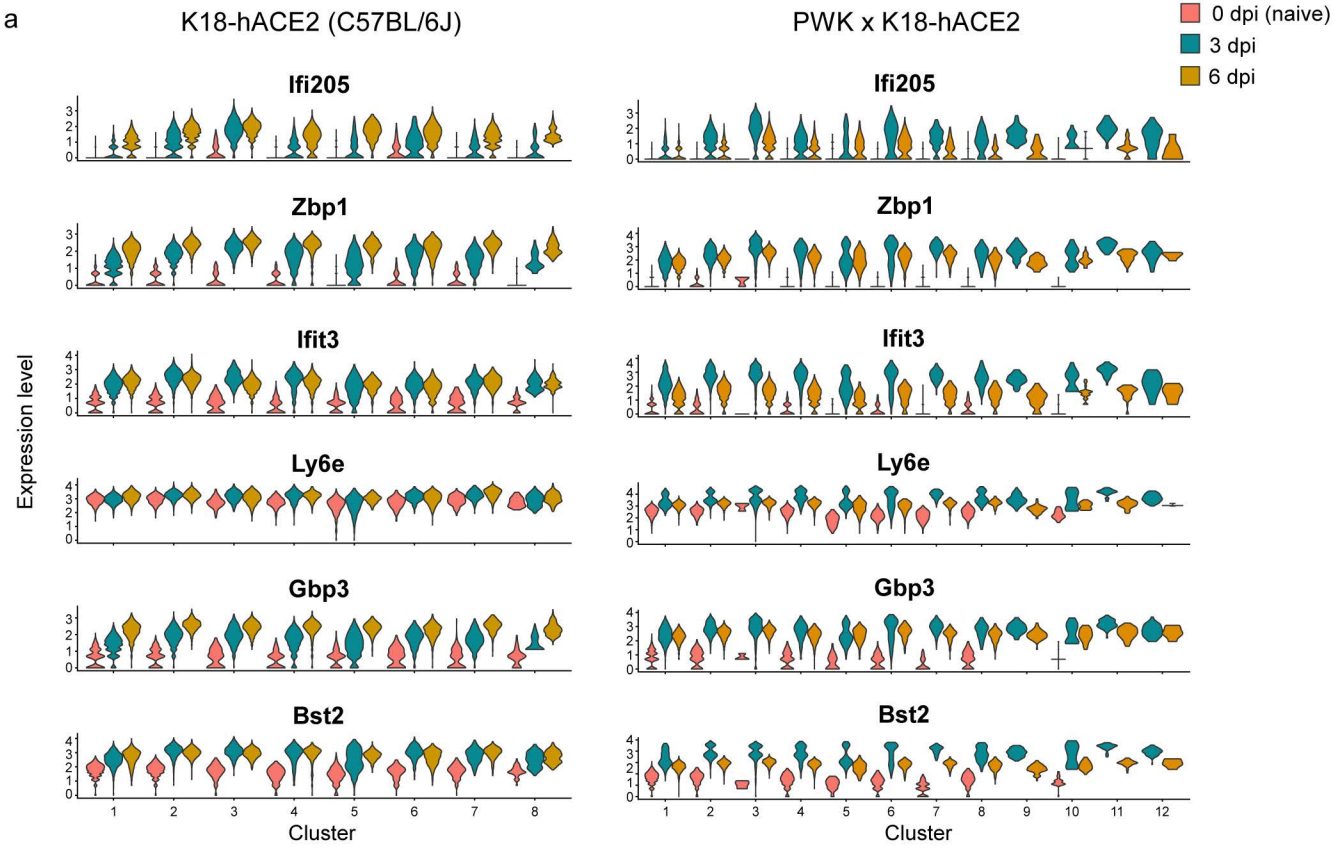
a
K18-hACE2 (C57BL/6J)
PWK x K18-hACE2
0 dpi (naive)
3 dpi
6 dpi
Ifi205
Zbp1
Ifit3
Ly6e
Gbp3
Bst2
Expression level
Cluster
Cluster

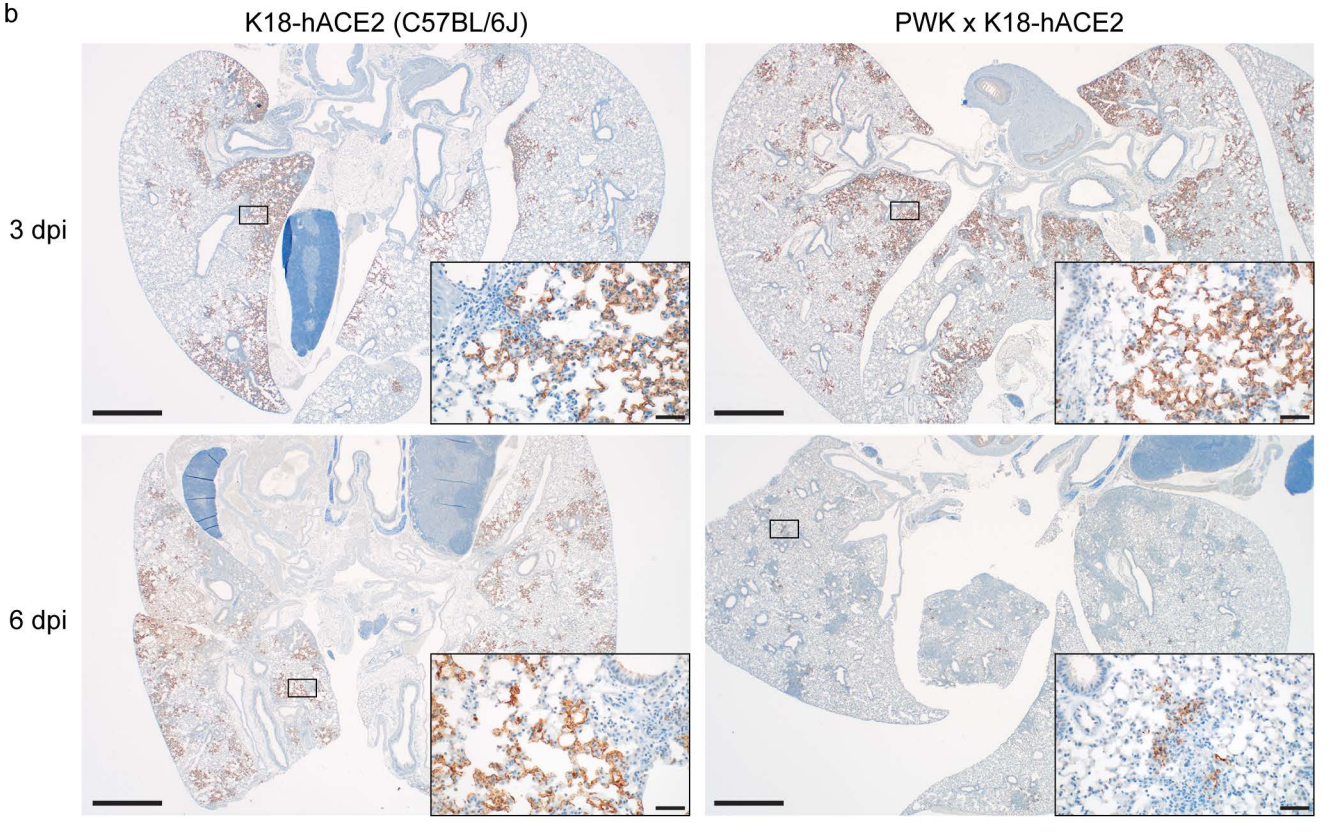
b
K18-hACE2 (C57BL/6J)
PWK x K18-hACE2
3 dpi
6 dpi

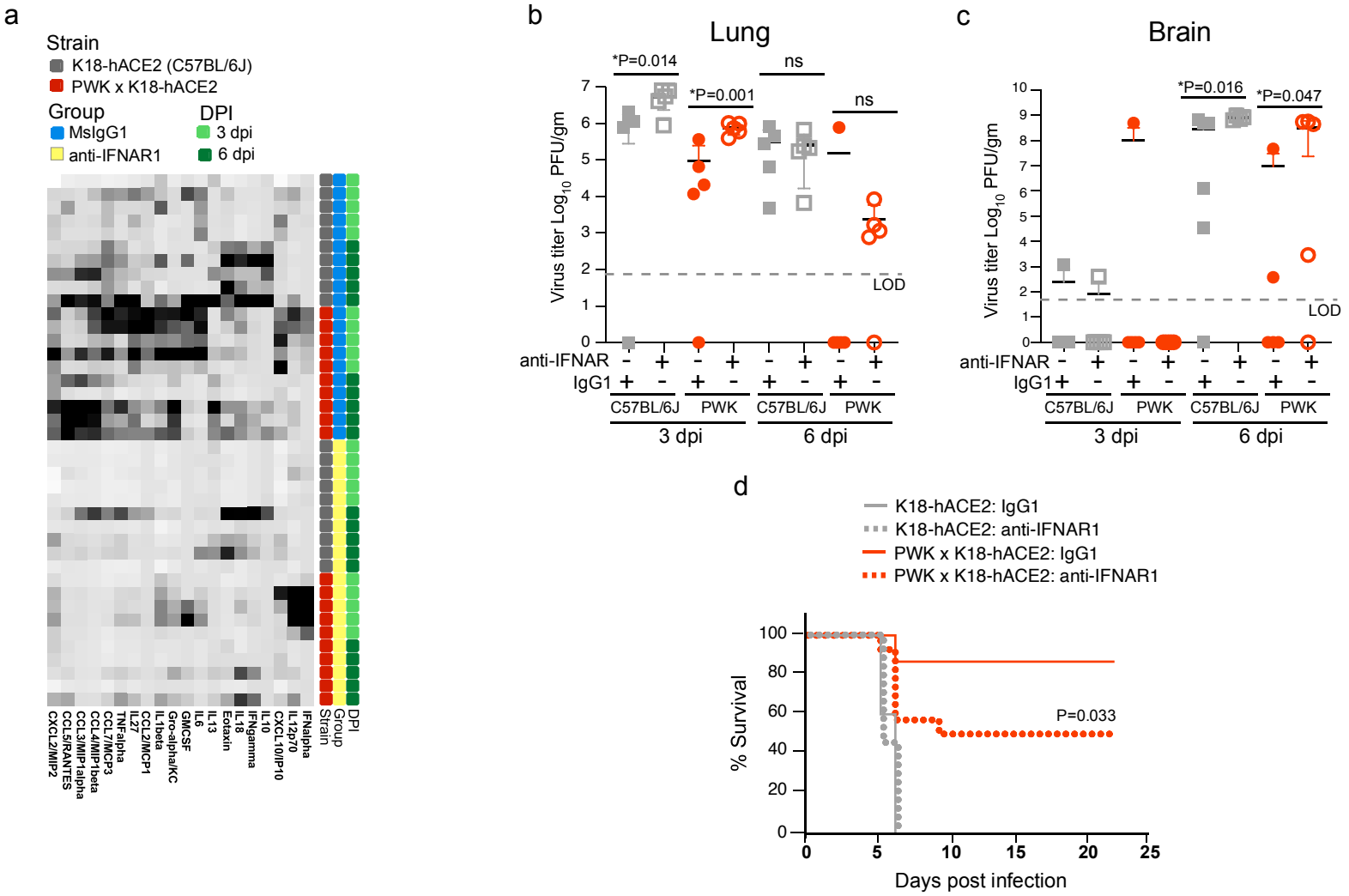
a
Strain
K18-hACE2 (C57BL/6J)
PWK x K18-hACE2
Group
MsIgG1
anti-IFNAR1
DPI
3 dpi
6 dpi
CXCL2/MIP2
CCL5/RANTES
CCL3/MIP1alpha
CCL4/MIP1beta
CCL7/MCP3
TNFalpha
IL27
CCL2/MCP1
IL1beta
Gro-alpha/KC
GMCSF
IL6
IL13
Eotaxin
IL18
IFNgamma
IL10
CXCL10/IP10
IL12p70
IFNalpha
Strain
Group
DPI
b
Lung
*P=0.014
*P=0.001
ns
ns
Virus titer Log10 PFU/gm
LOD
anti-IFNAR
IgG1
C57BL/6J
PWK
C57BL/6J
PWK
3 dpi
6 dpi
c
Brain
*P=0.016
*P=0.047
Virus titer Log10 PFU/gm
LOD
anti-IFNAR
IgG1
C57BL/6J
PWK
C57BL/6J
PWK
3 dpi
6 dpi
d
K18-hACE2: IgG1
K18-hACE2: anti-IFNAR1
PWK x K18-hACE2: IgG1
PWK x K18-hACE2: anti-IFNAR1
% Survival
P=0.033
Days post infection

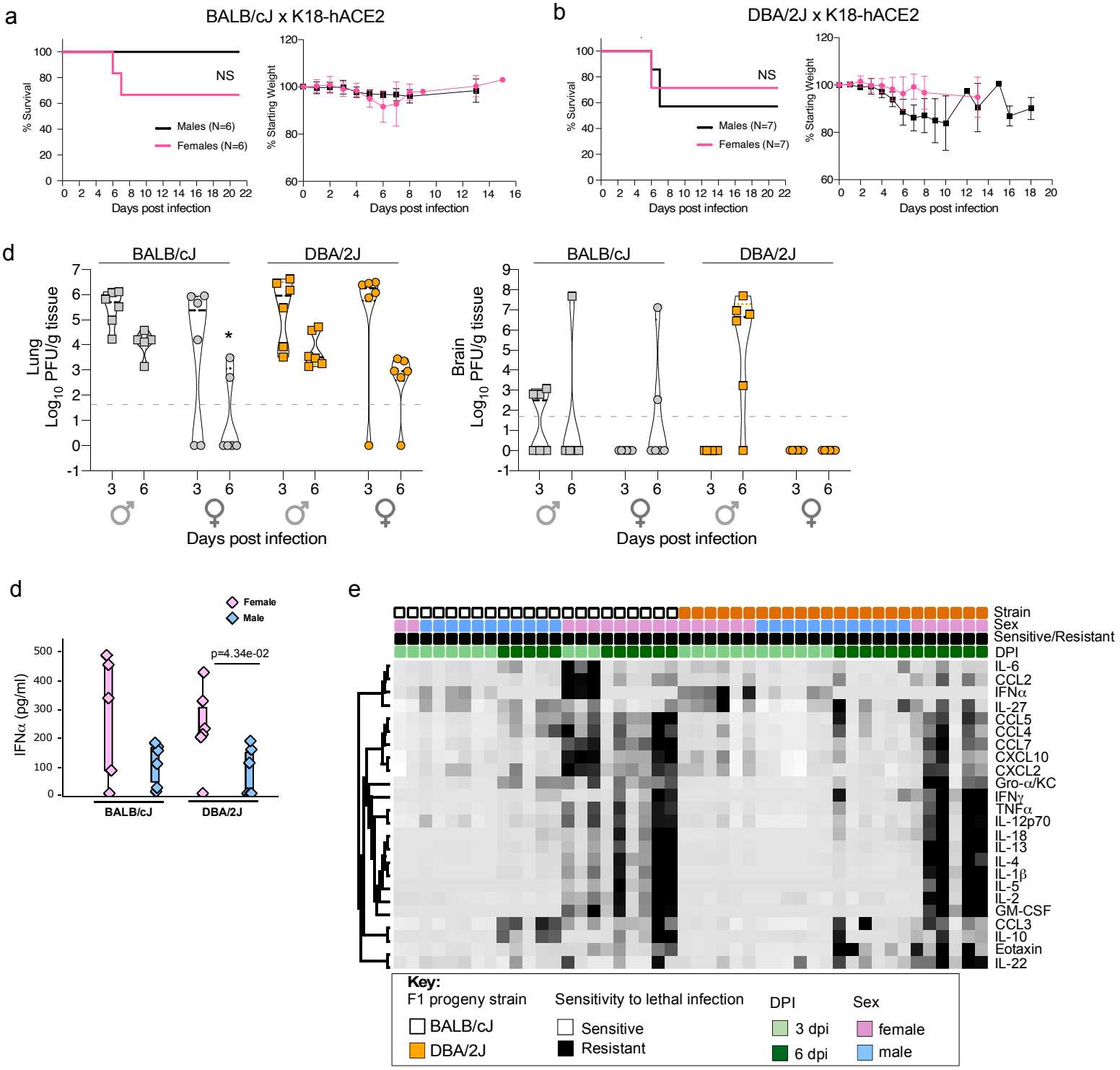
a
BALB/cJ x K18-hACE2
% Survival
NS
Males (N=6)
Females (N=6)
Days post infection
% Starting Weight
Days post infection
b
DBA/2J x K18-hACE2
% Survival
NS
Males (N=7)
Females (N=7)
Days post infection
% Starting Weight
Days post infection
d
BALB/cJ
DBA/2J
Lung
Log10 PFU/g tissue
*
Days post infection
BALB/cJ
DBA/2J
Brain
Log10 PFU/g tissue
Days post infection
d
Female
Male
IFNα (pg/ml)
p=4.34e-02
BALB/cJ
DBA/2J
e
Strain
Sex
Sensitive/Resistant
DPI
IL-6
CCL2
IFNα
IL-27
CCL5
CCL4
CCL7
CXCL10
CXCL2
Gro-α/KC
IFNγ
TNFα
IL-12p70
IL-18
IL-13
IL-4
IL-1β
IL-5
IL-2
GM-CSF
CCL3
IL-10
Eotaxin
IL-22
Key:
F1 progeny strain
BALB/cJ
DBA/2J
Sensitivity to lethal infection
Sensitive
Resistant
DPI
3 dpi
6 dpi
Sex
female
male

Fig. S1

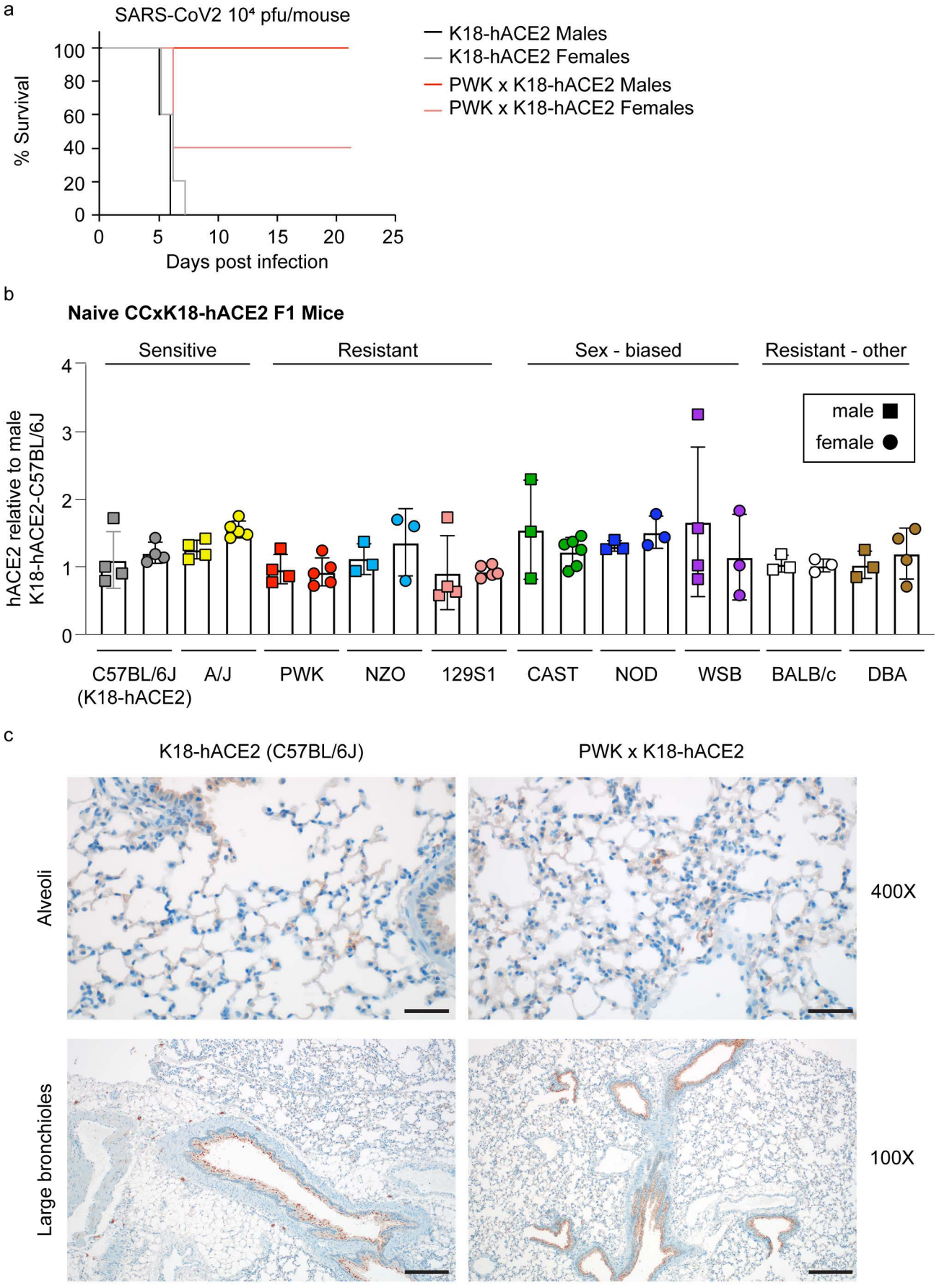
a
SARS-CoV2 10⁴ pfu/mouse
% Survival
100
80
60
40
20
0
0
5
10
15
20
25
Days post infection
K18-hACE2 Males
K18-hACE2 Females
PWK x K18-hACE2 Males
PWK x K18-hACE2 Females
b
Naive CCxK18-hACE2 F1 Mice
Sensitive
Resistant
Sex - biased
Resistant - other
hACE2 relative to male K18-hACE2-C57BL/6J
4
3
2
1
0
male
female
C57BL/6J (K18-hACE2)
A/J
PWK
NZO
129S1
CAST
NOD
WSB
BALB/c
DBA
c
K18-hACE2 (C57BL/6J)
PWK x K18-hACE2
Alveoli
400X
Large bronchioles
100X

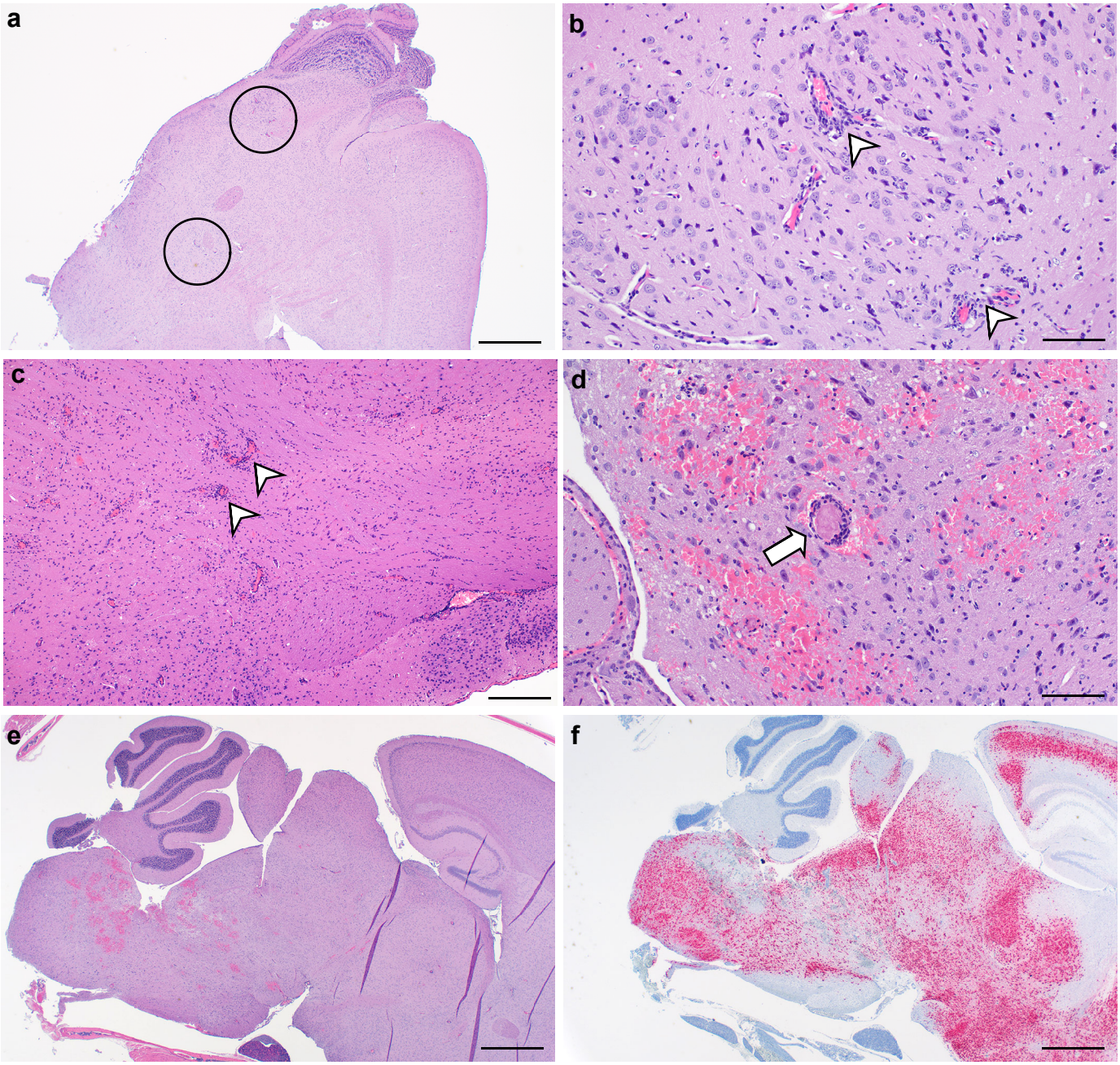
a
b
c
d
e
f

g

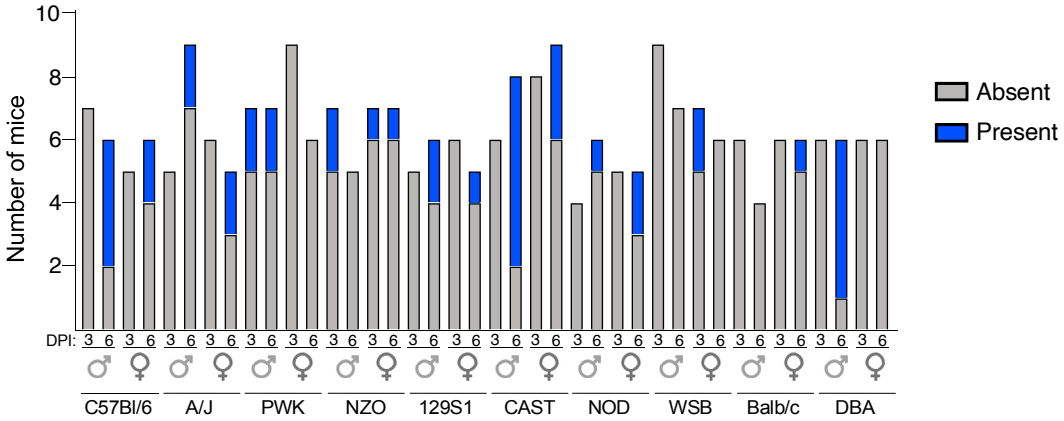
Number of mice
10
8
6
4
2
DPI: 3 6
♂ ♀
C57Bl/6
A/J
PWK
NZO
129S1
CAST
NOD
WSB
Balb/c
DBA
Absent
Present

Fig. S3

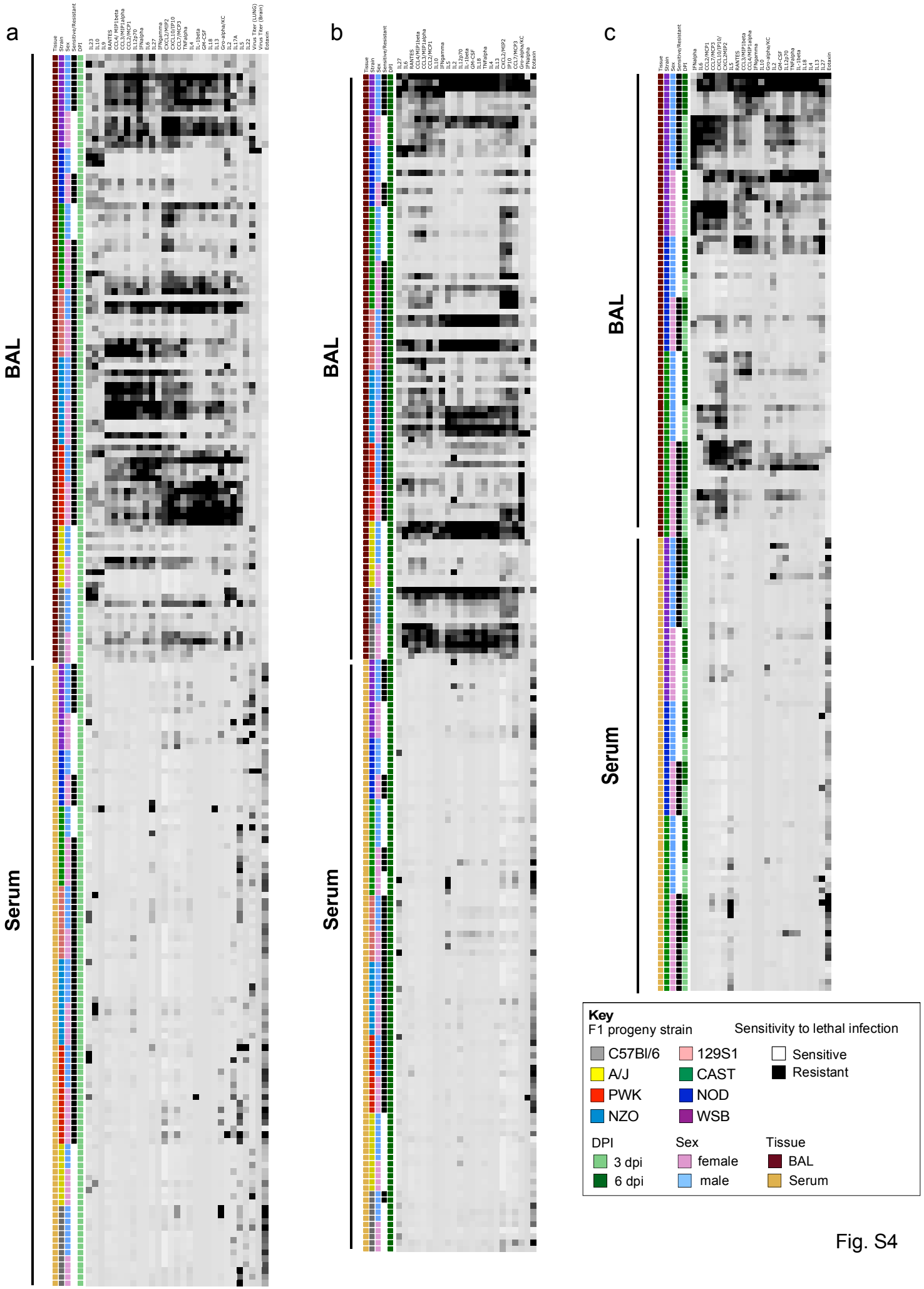
a
b
c
BAL
Serum
Key
F1 progeny strain
C57Bl/6
A/J
PWK
NZO
129S1
CAST
NOD
WSB
Sensitivity to lethal infection
Sensitive
Resistant
DPI
3 dpi
6 dpi
Sex
female
male
Tissue
BAL
Serum

Fig. S4

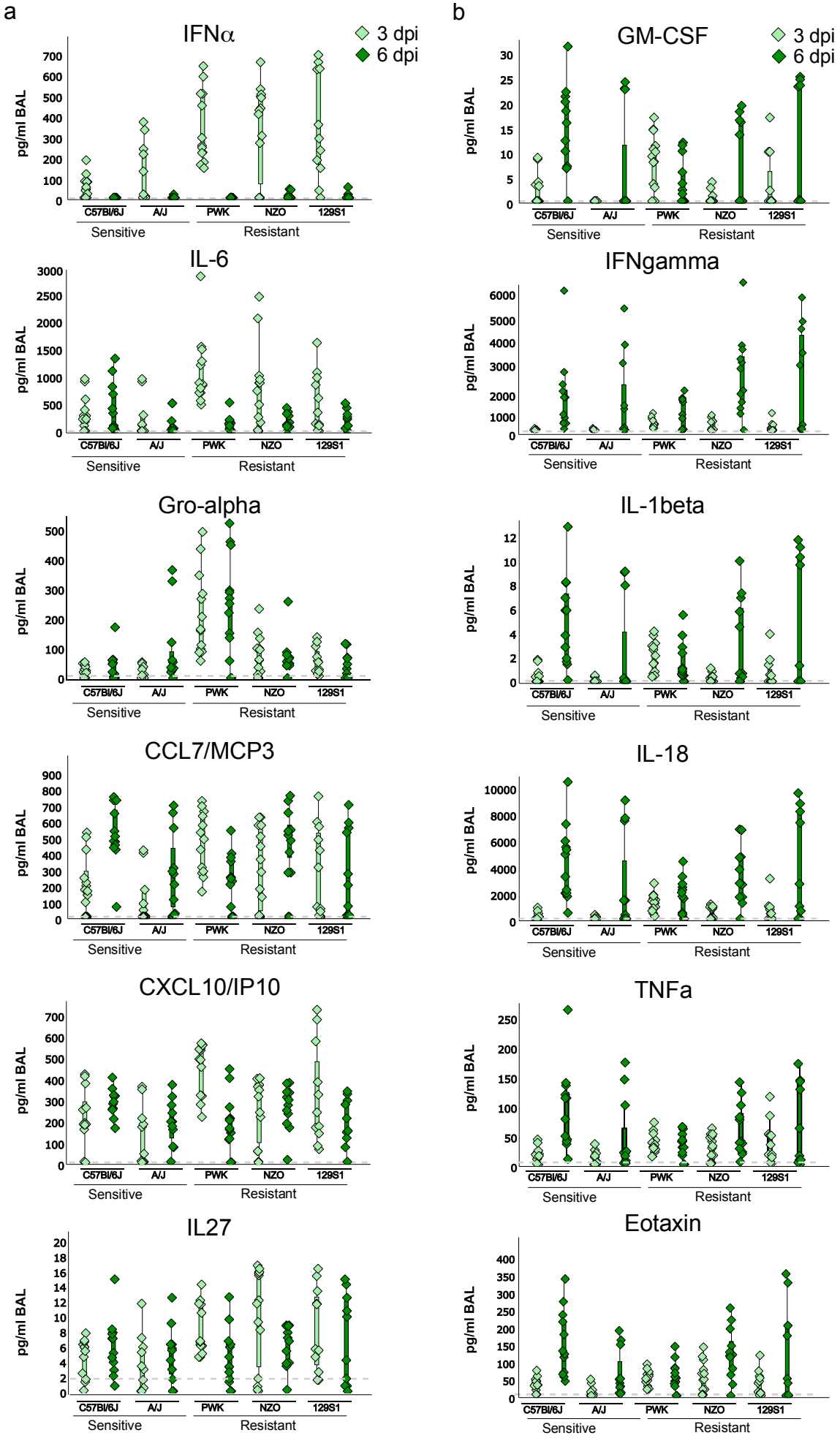
a
b
IFNα
GM-CSF
3 dpi
6 dpi
IL-6
IFNgamma
Gro-alpha
IL-1beta
CCL7/MCP3
IL-18
CXCL10/IP10
TNFa
IL27
Eotaxin
pg/ml BAL
C57Bl/6J
A/J
PWK
NZO
129S1
Sensitive
Resistant

Fig. S5

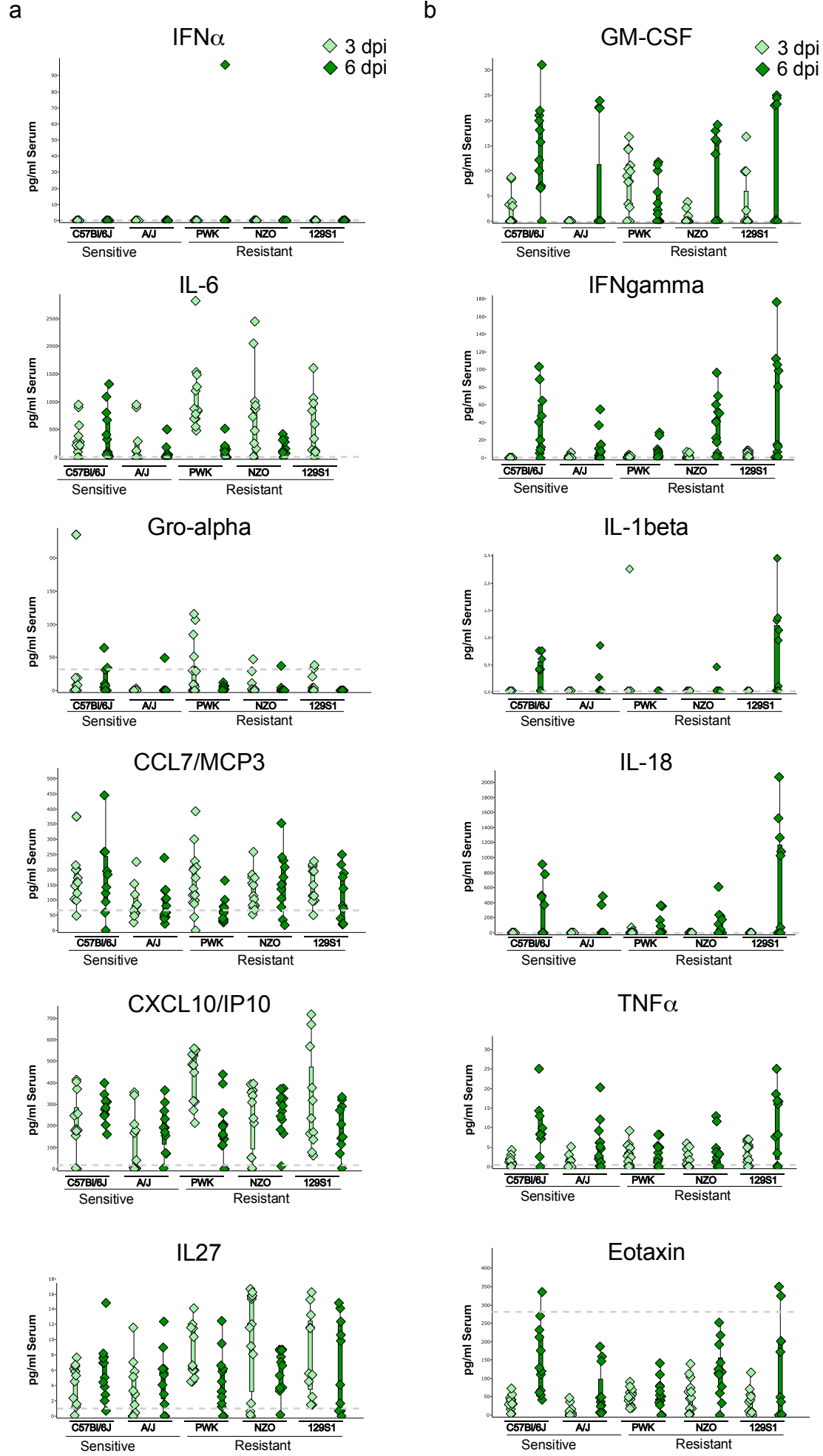
a
b
IFNα
GM-CSF
IL-6
IFNgamma
Gro-alpha
IL-1beta
CCL7/MCP3
IL-18
CXCL10/IP10
TNFα
IL27
Eotaxin
3 dpi
6 dpi
pg/ml Serum
C57Bl/6J
A/J
PWK
NZO
129S1
Sensitive
Resistant

Fig. S6

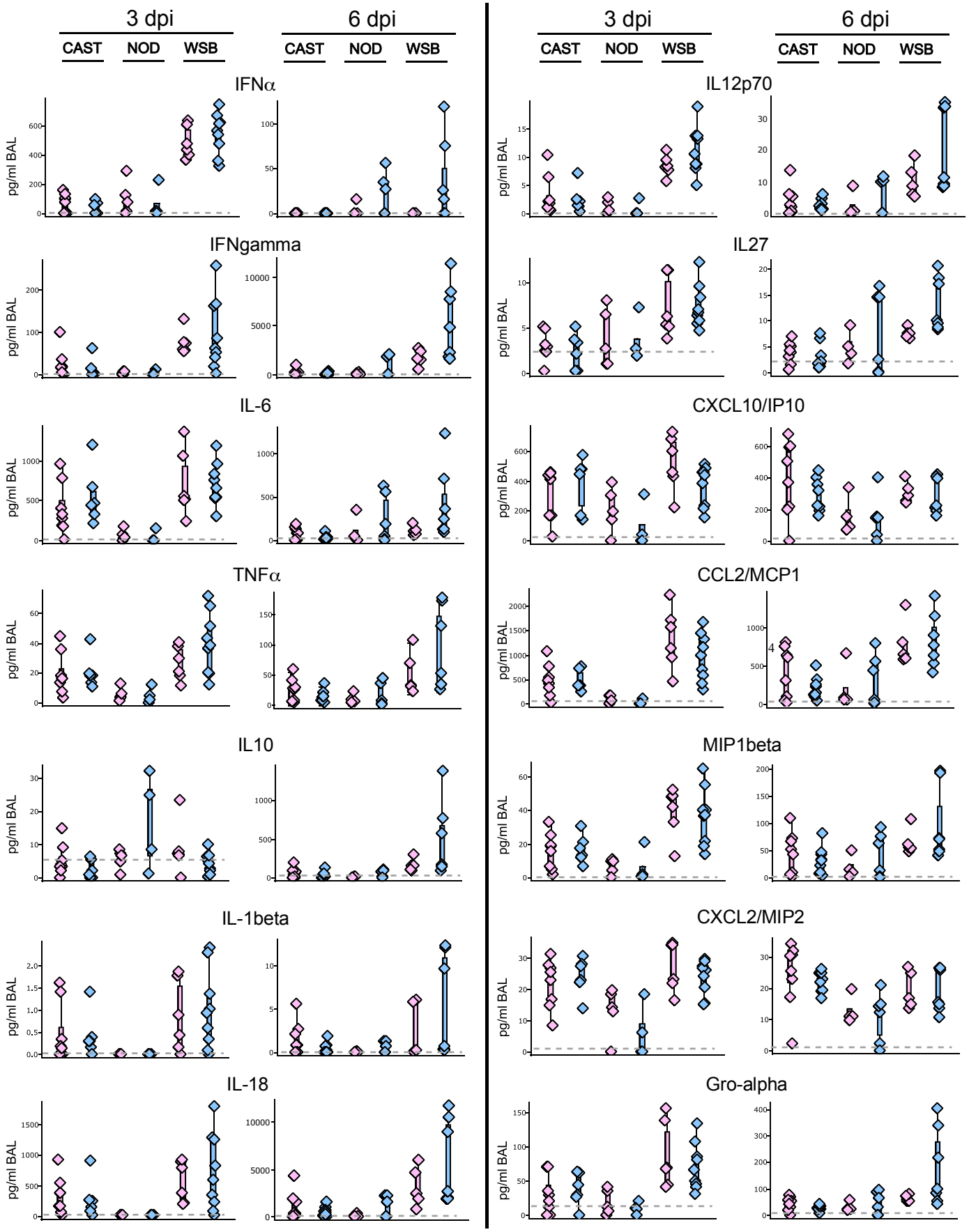
3 dpi
6 dpi
CAST
NOD
WSB
IFNα
IFNgamma
IL-6
TNFα
IL10
IL-1beta
IL-18
IL12p70
IL27
CXCL10/IP10
CCL2/MCP1
MIP1beta
CXCL2/MIP2
Gro-alpha
pg/ml BAL

Fig. S7